NASA TECHNICAL NOTE

NASA TN D-5722

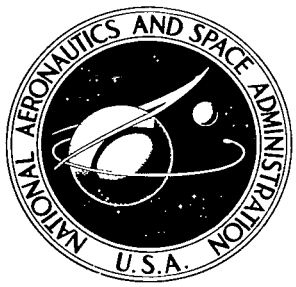

A STUDY OF RADIATION HEAT TRANSFER FROM A CYLINDRICAL FIN WITH BASE SURFACE INTERACTION

by Charles A. Cothran

George C. Marshall Space Flight Center
Marshall, Ala.

NATIONAL AERONAUTICS AND SPACE ADMINISTRATION • WASHINGTON, D. C. • APRIL 1970

1. REPORT NO. NASA TN D-5722	2. GOVERNMENT ACCESSION NO.	3. RECIPIENT'S CATALOG NO.
4. TITLE AND SUBTITLE A Study of Radiation Heat Transfer From a Cylindrical Fin With Base Surface Interaction		5. REPORT DATE April 1970 6. PERFORMING ORGANIZATION CODE
7. AUTHOR(S) Charles A. Cothran		8. PERFORMING ORGANIZATION REPORT # M362
9. PERFORMING ORGANIZATION NAME AND ADDRESS George C. Marshall Space Flight Center Marshall Space Flight Center, Alabama 35812 Astronautics Laboratory, Science and Engineering Directorate		10. WORK UNIT NO. 124-09-05-00-62 11. CONTRACT OR GRANT NO.
12. SPONSORING AGENCY NAME AND ADDRESS National Aeronautics and Space Administration Washington, D.C. 20546		13. TYPE OF REPORT & PERIOD COVERED Technical Note 14. SPONSORING AGENCY CODE

15. SUPPLEMENTARY NOTES
Submitted to the University of Alabama in partial fulfillment of the requirements for the Master of Science Degree in Engineering, August, 1969

16. ABSTRACT

This paper presents a study of the temperature distribution of a cylindrical fin transferring heat simultaneously by internal conduction and by surface radiation. The temperature distribution was studied considering the fin only and the more complex case of surface interactions with a circular base.

Equations are derived for the temperature distribution of the fin only, the fin with base surface interactions when both surfaces are black, and also the case of gray diffuse surfaces. Solutions to the equations are obtained by numerical techniques, the analysis is verified experimentally, and the results are given.

17. KEY WORDS Radiation Heat Transfer Base Surface Interaction Cylindrical Fin	18. DISTRIBUTION STATEMENT Unclassified - Unlimited		
19. SECURITY CLASSIF. (of this report) Unclassified	20. SECURITY CLASSIF. (of this page) Unclassified	21. NO. OF PAGES 93	22. PRICE * $3.00

*For sale by the Clearinghouse for Federal Scientific and Technical Information
Springfield, Virginia 22151

TABLE OF CONTENTS

LIST OF ILLUSTRATIONS

LIST OF ILLUSTRATIONS (Concluded)

LIST OF TABLES

NOMENCLATURE

A	Area (cm^2 or ft^2)
A'	That portion of a larger area that is viewed from a specified location (cm^2 or ft^2)
δA	Area with differential width and finite length
B	Radiosity (W/cm^2 or Btu/ft^2-hr)
B^*	Radiosity (dimensionless)
d( )	Differential
F	Configuration factor (dimensionless)
F^*	Configuration factor in terms of dimensionless parameters
g( )	Irradiation from surroundings (W/cm^2 or Btu/ft^2-hr)
H	Irradiation from the system (W/cm^2 or Btu/ft^2-hr)
H^*	Irradiation from the system (dimensionless)
$\hat{i}, \hat{j}, \hat{k}$	Unit vectors
k	Thermal conductivity (W/cm-°K or Btu/ft-hr-°R)
l, m, n	Direction cosines
L	Length (cm)
M	Number of isothermal segments of the specimen
N_c	Conduction parameter (dimensionless)
N	$N_c \epsilon_R / \rho'_R$
N'	$N_c \epsilon_R$
$\hat{n}$	Unit vector normal to a surface

NOMENCLATURE (Continued)

q	Rate of heat flow (W)
R	Dimensionless ratio, r/L
r	Radius (cm)
$\bar{S}$	Line
$\hat{S}$	Vector
S	Magnitude of line $\bar{S}$
T	Absolute temperature (degrees Kelvin, °K)
X	Matrix of $\dfrac{\delta_{ij} - (1 - \epsilon_i)}{\epsilon_i} F_{\delta A_i - \delta A_j}$ for $1 \leq i \leq M$
x, y, z	Rectangular coordinates
Z	Dimensionless ratio, z/L
α	Absorptivity (dimensionless)
δ_{ij}	Kronecker delta
ϵ	Emissivity (dimensionless)
η	Efficiency (dimensionless)
θ	Dimensionless temperature, T/T_0
π	3.14159
ρ	Cylindrical radius coordinate
ρ'	Reflectivity (dimensionless)
σ	Stefan-Boltzmann constant (5.6699×10^{-12} W/cm^2-°K^4 or 0.1713×10^{-8} Btu/ft^2-hr-°R^4)
τ, τ'	Dummy integration variables

NOMENCLATURE (Concluded)

φ	Cylindrical coordinate angle
ψ	Inverse of X

Subscripts:

B	Base surface
i, j	i denotes a specific element of j elements
R	Rod surface
δA	Differential strip area
dA	Differential area
0, 1, 2.. 11	Thermocouple station locations on the rod test specimen

ACKNOWLEDGMENT

The author would like to take this opportunity to acknowledge the contributions of those persons whose assistance was most prominent in the preparation of this thesis. Sincere thanks are extended to Dr. A. R. Shouman for his many helpful comments and for his efforts in sponsoring the use of the MSFC Propulsion and Vehicle Engineering Laboratory test equipment and facilities. Sincere thanks are also extended to Dr. R. Blanton, his thesis advisor, for his many helpful comments and his guidance and to Miss Lucy Coward of the MSFC Computation Laboratory who programmed the numerical solutions of the temperature distribution equations.

A STUDY OF RADIATION HEAT TRANSFER FROM A CYLINDRICAL FIN WITH BASE SURFACE INTERACTION

SUMMARY

In this study the temperature distribution and heat transfer rates of a cylindrical radiating fin were investigated, considering no base surface interaction and also the case of interaction with a circular base. Surroundings of the fin were assumed to be black and at a temperature of absolute zero.

The equations governing the temperature distribution of a fin attached to a circular base causing radiation interaction were derived for two cases: when their surfaces were black; and when their surfaces were gray and diffuse. Solutions to the equations were obtained by numerical techniques and the analysis was qualitatively verified with experimental studies.

Numerical solutions were obtained for the specific conditions of each of the 20 test runs and for a wide variation of the governing parameters for a black rod and base. The parameter study showed that the rod heat transfer efficiency may vary as much as 50% with changing base size. The experimental data and numerical solutions showed trend agreement. However, it was shown that substantial error in the measured temperature distribution could be attributed to the use of an excessive number of thermocouples and the carbon coating used during ten of the tests.

INTRODUCTION

The subject of heat transfer from fins and extended surfaces has been studied analytically and experimentally for almost two centuries [1]. Until recent years most work was concentrated on convection from fins with constant thermal properties. The problem of a fin exchanging heat with its surroundings by radiation has only recently come under extensive study as a result of man's interest in space and the newly found capability for space travel.

The temperature distribution along a thin rod, wire, or thin-walled tube heated by an electric current while in a vacuum has been of interest, both experimentally and theoretically, for a long time. The literature on this problem contains work by Langmuir [2], Langmuir and Taylor [3], Worthing [4], Worthing and Holliday [5], Stead [6], Bush and Gould [7], Baerwald [8], Jain and Krishman [9], and Shouman [10]. Shouman [10] presented an exact solution for a one-dimensional fin with constant cross sectional area and constant thermal properties that transferred heat from its surface by radiation only to an equivalent sink temperature.

The interest in space exploration generated an interest in fins of various geometries applicable to heat exchanger designs. The early published work in this area treated the temperature distribution of isolated fins. Lieblien [11] analyzed the temperature distribution along a rectangular fin and Chambers and Somers [12] presented a similar analysis of a circular

fin. Tatom [13] presented the mathematical formulation for the temperature distribution along a rod and presented an exact solution for the special case of an infinitely long rod.

The analysis of fins then proceeded to the consideration of mutual irradiation of fins and their base surfaces. Callinan and Berggren [14] considered a wide range of design problems and studied the fin geometry shown in Figure 1A; however, the base surface effect and multiple reflections were not considered. Bartas and Sellers [15] indicated the importance of radiation interaction for this design and considered a singly reflected ray in the analytical formulation but omitted the singly reflected ray for the solutions presented.

The problem of flat rectangular fins sharing a common edge, Figure 1B, was studied by Sparrow, Eckert, and Irvine [16]. These authors formulated the solutions for this geometry, and in another study [17], they presented solutions for mutual irradiation between fins whose surfaces are gray and reflect diffusely. A similar arrangement, but of trapezoidal cross section, was considered by Karlekar and Chao [18]; they presented an optimization procedure for achieving maximum dissipation. Hering [19] studied this fin system and presented solutions for gray surfaces which reflect specularly, and he compared the effectiveness of the cases of specular and diffuse reflections.

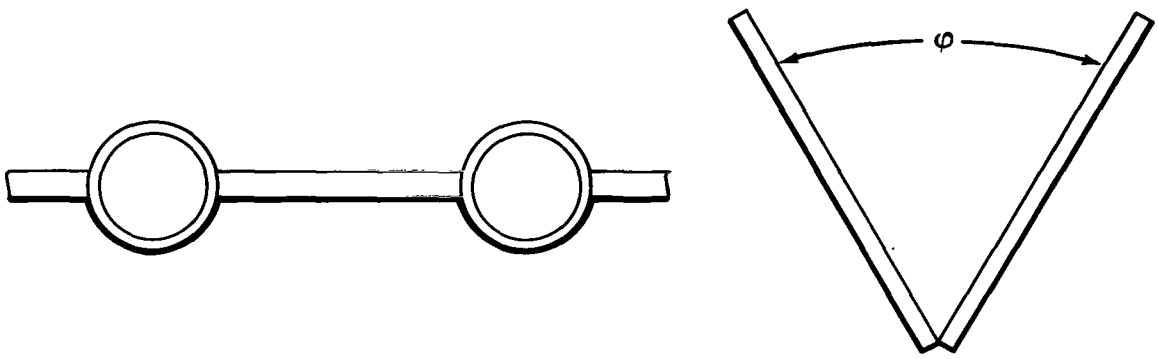

(A) (B)

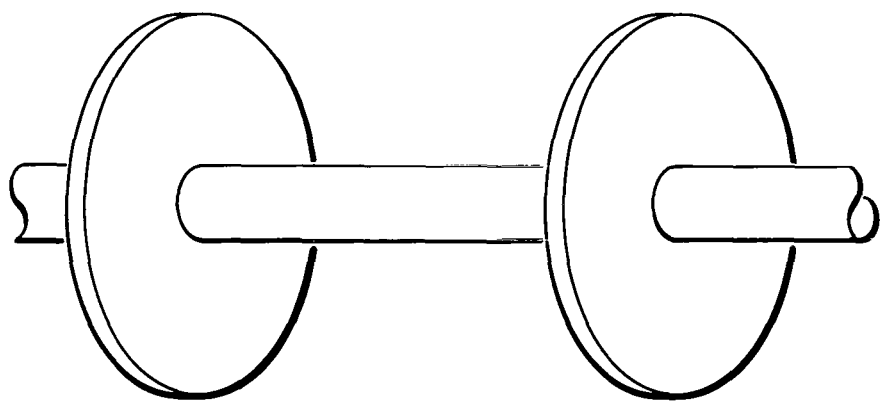

(C)

FIGURE 1. FIN SYSTEM GEOMETRIES

A complete mathematical formulation of the governing equations for the system shown in Figure 1A was presented by Sparrow and Eckert [20]. They considered the mutual irradiation between the fin and base surfaces and irradiation from external sources. The case of selective gray surfaces was also considered. However, the solutions presented were for black surfaces with negligible irradiation from external sources. The physical parameters were varied over a wide range and the conduction parameter, N_c, was varied from 0.5 to 20. Sarabia and Hitchcock [21] presented the solutions for this system in terms of overall fin-tube efficiency for the black and gray diffuse cases. The conduction parameter was varied from 1 to 20 for the black case and the data were presented for $N_c = 1$ for the gray diffuse case. Hwang-Bo [22] also considered this sytem and presented a method of maximizing heat rejection per unit weight; however, irradiation was simplified by neglecting components reflected twice or more.

Sparrow, Miller and Jonsson [23] studied the fin system shown in Figure 1C with gray diffuse surfaces. The system consisted of annular fins mounted on a constant temperature tube with mutual irradiation between the fins and the tube. The problem was solved for a wide range of physical parameters, and the conduction parameter was varied from 0 to 0.7.

The effects of convection were considered negligible in the previously mentioned papers and were neglected for this study. Gordon [24] substantiated that convection was negligible at pressures below 10^{-4} millimeters of mercury.

The mathematical formulation of the energy balance on a differential element of a fin transferring heat by internal conduction and by surface radiation results in a second order nonlinear differential equation. The equation is further complicated when the mutual irradiation by the fin base surface, other fins, and external sources are considered. As a result of these complications, an exact solution is not known and numerical techniques must be employed. An exact solution for a fin not considering interaction with other surfaces has been published by Shouman [10]. In a test program to verify his solution for the temperature distribution of a fin, Shouman used an aluminum rod 2.54 cm (1 inch) in diameter and 48.90 cm ($19\frac{1}{4}$ inches) long. As an extension of this work it was decided to investigate, both analytically and experimentally, the effect of adding a base surface upon the temperature distribution of the radiating rod.

ANALYSIS

Formulation of Equations for Black Surfaces

The following analysis considered the heat transferred from a black circular rod including interaction with a black base surface. The base surface considered was circular with a uniform temperature. The temperature gradient in the fin was assumed extremely small in the radial direction compared to the gradient in the z direction which reduced the problem to one-

dimensional heat flow in the rod. In addition, the following assumptions were made:

1. The rod was isotropic and homogeneous.
2. The material thermal properties were constant.
3. There were no heat sources or sinks in the rod.
4. The system and surroundings were at thermal equilibrium.

Now consider a differential slice of the rod shown in Figure 2A and C at a distance z from the base. The net heat, q, conducted into the element dz

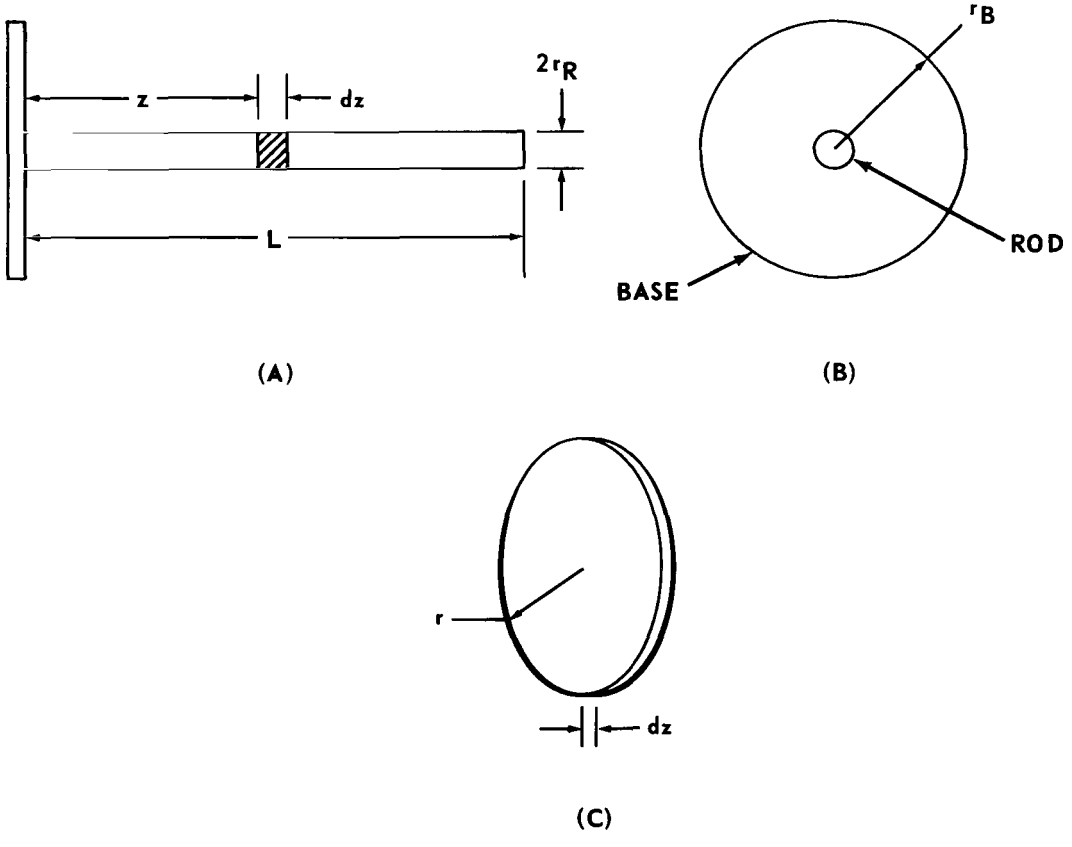

FIGURE 2. SKETCH OF ROD-FIN WITH CIRCULAR BASE

was equated to the heat lost by radiation, or

$$\left(dq_{\text{conduction}}\right)_{\text{Net}} = \left(dq_{\text{radiation}}\right)_{\text{Net}} \tag{II-1}$$

The amount of heat that entered the element at z by conduction was

$$q_{(z)} = -\pi r_R^2 \left(k \frac{\partial T}{\partial z}\right) \tag{II-2}$$

where T represented the absolute temperature and k, the thermal conductivity. To determine the corresponding quantity of heat conducted from the element at $z + dz$, let $q(z, T) = k \frac{\partial T}{\partial z}$ and allow z to increase by dz. Then when $q(z + dz, T)$ was expanded in a Taylor's series and all terms after the first two were neglected [25],

$$q(z + dz, T) = q(z, T) + \frac{\partial q(z, T)}{\partial z} dz \tag{II-3}$$

or

$$q(z + dz, T) = k \frac{\partial T}{\partial z} + \frac{\partial}{\partial z}\left(k \frac{\partial T}{\partial z}\right) dz \tag{II-4}$$

Then, the heat conducted at $z + dz$ was

$$dq_{(z + dz)} = -\pi r_R^2 \left[k \frac{\partial T}{\partial z} + \frac{\partial}{\partial z}\left(k \frac{\partial T}{\partial z}\right) dz\right] \tag{II-5}$$

and the net conduction into the element was

$$\left(dq_{conduction}\right)_{Net} = \pi\, r_R^2 \left[\frac{\partial}{\partial z}\left(k\frac{\partial T}{\partial z}\right) dz\right] \qquad \text{(II-6)}$$

or

$$\left(dq_{conduction}\right)_{Net} = \pi\, r_R^2\, k\frac{\partial^2 T}{\partial z^2}\, dz \qquad \text{(II-7)}$$

since k was assumed constant.

When the radiation from the fin was considered, there were three possibilities:

1. The surface of the element emitted a quantity of radiant energy

$$\sigma\, T^4\, (2\pi r_R dz), \qquad \text{(II-8)}$$

where σ was the Stefan-Boltzman constant.

2. There was a quantity of energy incident on the element due to the base surface. When the configuration factor, F, which denotes the fraction of energy leaving one surface which was incident on another was introduced, the base surface contribution became

$$-\left(\sigma\, T_B^4\, A_B\right) F_{A_B - \delta A_R} \qquad \text{(II-9)}$$

and when the reciprocity relationship between configuration factors,

$$A_B F_{A_B - \delta A_R} = 2\pi r_R dz \; F_{\delta A_R - A_B}, \tag{II-10}$$

was used the energy incident on the element of rod from the base was written as

$$-\sigma T_B^4 \; (2\pi r_R dz) \; F_{\delta A_R - A_B} \cdot \tag{II-11}$$

3. There was a quantity of energy from some external source. Since the base surface would probably block a portion of any energy from an external source, the incident energy would vary with z. When the external radiation was defined as g(z) per unit area, the quantity incident on the element dz was

$$-g(z) \; 2\pi r_R dz. \tag{II-12}$$

The net radiation transfer was written as

$$\left(dq_{\text{radiation}}\right)_{\text{Net}} = \left[\sigma T^4 - \sigma T_B^4 \; F_{\delta A_R - A_B} - g(z)\right] \; 2\pi r_R dz. \tag{II-13}$$

When combined, the net conduction and the net radiation transfer yielded

$$\frac{r_R}{2} \; k \frac{\partial^2 T}{\partial z^2} = \sigma T^4 - \sigma T_B^4 \; F_{\delta A_R - A_B} - g(z) \tag{II-14}$$

which was written as

$$\frac{d^2T}{dz^2} = \frac{2\sigma}{r_R k}\left[T^4 - T_B^4 F_{\delta A_R - A_B}\right] - \frac{2g(z)}{r_R k} \quad . \tag{II-15}$$

The incident energy from the surroundings may be neglected if the rod temperature is sufficiently high compared to the surrounding temperature. Since the tests were conducted with the surroundings at the temperature of liquid nitrogen, the term for incident energy was neglected.

The differential equation for the temperature distribution in the rod was written in dimensionless form by introducing the following nondimensional quantities,

$$\theta = \frac{T}{T_0}, \quad \theta_B = \frac{T_B}{T_0}, \quad Z = \frac{z}{L}, \quad R_1 = \frac{r_R}{L}, \text{ and } R_2 = \frac{r_B}{L} .$$

Substitution into equation (II-15) and neglect of g(z) yielded

$$\frac{d^2(T_0\theta)}{d(ZL)^2} = \frac{2\sigma}{r_R k}\left[(T_0\theta)^4 - (T_0\theta_B)^4 F^*_{\delta A_R - A_B}\right] \tag{II-16}$$

which reduced equation (II-16) to

$$\frac{d^2\theta}{dZ^2} = \frac{2\sigma L^2 T_0^3}{r_R k}\left[\theta^4 - \theta_B^4 F^*_{\delta A_R - A_B}\right] . \tag{II-17}$$

The quantity $\frac{2\sigma L^2 T_0^3}{r_R k}$ was defined as N_c and is generally referred to as the conduction parameter in the literature. The above equation then became

$$\frac{d^2\theta}{dZ^2} = N_c\left[\theta^4 - \theta_B^4 F^*_{\delta A_R - A_B}\right] . \tag{II-18}$$

The term θ_B was equal to 1 at $Z = 0$ when the rod temperature was equal to the base temperature. For the tests conducted, however, θ_B was not equal

to 1. The derivation of the configuration factor $F^*_{\delta A_R - A_B}$ was quite lengthy and is presented in detail in Appendix A.

The expression for the temperature distribution from a black rod viewing a black circular base was completed by defining the boundary conditions: at $z = 0$ the temperature $T = T_0$ and at $z = L$, $\frac{dT}{dz} = 0$ and correspondingly $\theta = 1$ at $Z = 0$ and $\frac{d\theta}{dZ} = 0$ at $Z = 1$.

The heat transferred from the rod was found quite simply since at thermal equilibrium the heat loss from the rod surface must be equal to the amount of heat conducted into the rod at the base, or

$$q_{conduction} = \left(q_{radiation}\right)_{Net} = q_R \tag{II-19}$$

or

$$q_R = - k(\pi r_R^2) \left(\frac{dT}{dz}\right)_{z=0}. \tag{II-20}$$

When the above equation was written in terms of the dimensionless variables θ, Z, and N_c, the expression for q_R became

$$\frac{q_R}{\sigma T_0^4 (2\pi r_R L)} = - \frac{1}{N_c} \left(\frac{d\theta}{dZ}\right)_{Z=0}. \tag{II-21}$$

Examination of the left-hand side of the above equation revealed that the quantity was the ratio of the actual fin heat transferred to the heat transferred from an ideal fin which was the fin efficiency, η.

Numerical Solution for Black Surfaces

The equation (II-18) for the temperature distribution was solved numerically using the Runge-Kutta method. It was solved by determining which of a succession of guessed values of $\frac{d\theta}{dZ}$ at $Z = 0$ led to a solution that satisfied the boundary condition $\frac{d\theta}{dZ} = 0$, at $Z = 1$. A ΔZ step size of 0.01 was used for all solutions; however, ΔZ step sizes of 0.001 and 0.0001 were tried and it was determined that the accuracy was not improved. Solutions were determined for each of the test cases and also for a wide selection of N_c and the dimensionless ratios, $R_1 = \frac{r_R}{L}$ and $R_2 = \frac{r_B}{L}$, which governed the configuration factor, $F_{\delta A_R - A_B}$. These data are presented in the curves in Appendix C and typical values of $\theta(Z)$ are presented in Table C-1 of Appendix C.

Since the Runge-Kutta integration of equation (II-18) yielded $\left(\frac{d\theta}{dZ}\right)_{Z=0}$, the fin efficiency ($\eta$) or the fin heat transfer (q_R) was easily obtained from equation (II-21). The fin efficiency was plotted versus the conduction parameter for the limiting cases of $R_2 = R_1$ (no base), $R_2 = \infty$ (infinite base, $F_{\delta A_R - A_B} = 0.5$) and two intermediate values of R_2 for each of five values of R_1. The results are plotted in Appendix C.

Formulation of Equations for Nonblack Surface

In this section the analysis is extended from the black case to the case of gray, diffuse emitters and absorbers. When a surface element on the rod a distance z from the base is considered, the energy that leaves this location

includes both the direct emission and the reflected incident energy. This is called the radiosity B (energy/unit area-time),

$$B = \epsilon\sigma T_R^4 + \rho' H \qquad \text{(II-22)}$$

where H is the incident energy per unit time, and ϵ and ρ' are the emissivity and reflectivity, respectively.

The net heat loss from a surface location was B - H and the fin energy balance was,

$$\frac{d^2T}{dz^2} = \frac{2}{kr_R}(B_R - H_R) \qquad \text{(II-23)}$$

where the conduction was evaluated the same as in the black analysis. T and Z were normalized as before

$$\theta = \frac{T}{T_0} \text{ and } Z = \frac{z}{L}$$

which yielded

$$\frac{d^2\theta}{dZ^2} = \frac{2\,L^2}{kr_R T_0}(B_R - H_R)\ . \qquad \text{(II-24)}$$

When equation (II-24) was multiplied and divided by σT_0^4, and B^* and H^* were defined as $B^* = \frac{B}{\sigma T_0^4}$ and $H^* = \frac{H}{\sigma T_0^4}$, then

$$\frac{d^2\theta}{dZ^2} = N_c (B_R^* - H_R^*)\,. \qquad \text{(II-25)}$$

The irradiation H_R^* was a function of the base surface radiosity and of the radiation from the surroundings; thus

$$H_R^* = \frac{g(Z)}{\sigma T_B^4} + \int_{A_B} B_B^* F^*_{\delta A_R - \delta A_B} \cdot \tag{II-26}$$

When selective surfaces were not considered, then

$$B_R^* = \epsilon_R \theta^4 + \rho'_R H_R^* \tag{II-27}$$

where ϵ and ρ were gray body properties, that is,

$$\epsilon = \alpha = 1 - \rho' \, . \tag{II-28}$$

The radiosity distribution B_B^* in equation (II-26) was related to the other energy transfers of the system by the following radiant flux balance

$$B_B^* = \epsilon_B \theta_B^4 + \rho' \left[\frac{g(Z)}{\sigma T_0^4} + \int_{A_R} B_R^* F^*_{\delta A_B - \delta A_R} \right] . \tag{II-29}$$

The four equations (II-25), (II-26), (II-27), and (II-29) in four unknowns described the temperature distribution of the rod. However, H_R^* was eliminated by use of equation (II-27).

$$H_R^* = \frac{B_R^* - \epsilon_R \theta^4}{\rho'_R} \, . \tag{II-30}$$

Substitution into equation (II-25) yielded

$$\frac{d^2\theta}{dZ^2} = \frac{N_c \epsilon_R}{\rho'_R} \left[\theta^4 - B_R^* \right] , \tag{II-31}$$

and similarly equation (II-26) yielded

$$B_R^* = \epsilon_R \theta^4 + \frac{\rho'_R g(Z)}{\sigma T_0^4} + \rho'_R \int_{A_B} B_B^* F^*_{\delta A_R - \delta A_B} \cdot \tag{II-32}$$

This yielded three equations in three unknowns, B_R^*, B_B^*, and $\theta(Z)$, the temperature distribution, which were to be determined.

The problem was completed by defining the boundary conditions. At $z = 0$ the temperature $T = T_0$, and at $z = L$, $\frac{dT}{dz} = 0$. Correspondingly, $\theta = 1$ at $Z = 0$, and $\frac{d\theta}{dZ} = 0$ at $Z = 1$. This nonlinear system of differential and integral equations required a simultaneous solution.

Since the case being considered had negligible incident radiant energy, $g(Z) \approx 0$, the system of equations was reduced to

$$\frac{d^2\theta}{dZ^2} = \frac{N_c \epsilon_R}{\rho'_R} \left[\theta^4 - B_R^*\right] \tag{II-33}$$

$$B_B^* = \epsilon_B \theta_B^4 + \rho'_B \int_{A_R} B_R^* F^*_{\delta A_B - \delta A_R} \tag{II-34}$$

$$B_R^* = \epsilon_R \theta^4 + \rho'_R \int_{A_B} B_B^* F^*_{\delta A_R - \delta A_B} \tag{II-35}$$

There were no known exact analytical solutions and therefore a numerical solution was sought.

Numerical Solution for Nonblack Surfaces

The above system of equations could have been solved numerically in this form by assuming distributions for B_R^* and B_B^* and iterating until the boundary conditions were satisfied. This would have been quite tedious, however, since equations (II-34) and (II-35) must first be satisfied. Then, B_R^* must be substituted into equation (II-33) to find $\theta(Z)$ which must be used as an input into equations (II-34) and (II-35) until agreement is reached.

This process must be repeated until the boundary conditions are satisfied. Because of the lengthy iteration involved in solving the system in this form, it was more expeditious to convert equation (II-33) into an integral form which included the boundary conditions.

When N was defined as

$$N = \frac{N_c \epsilon_R}{\rho'_R} , \tag{II-36}$$

equation (II-33) became

$$\frac{d^2\theta(Z)}{dZ^2} = N\left[\theta^4(Z) - B^*_R(Z)\right] . \tag{II-37}$$

The above equation was integrated from 1 to Z and the boundary condition $\left(\frac{d\theta}{dZ}\right)_{Z=1} = 0$ applied to yield

$$\frac{d\theta(Z)}{dZ} = N\int_1^Z \left[\theta^4(\tau) - B^*_R(\tau)\right] d\tau \tag{II-38}$$

where τ was a dummy integration variable. Equation (II-38) was integrated from 0 to Z and the boundary condition $\theta = 1$ at $Z = 0$ was applied to yield

$$\theta(Z) = 1 + N\int_0^Z \int_1^{\tau'} \left[\theta^4(\tau) - B^*_R(\tau)\right] d\tau\, d\tau'. \tag{II-39}$$

The above double integral was transformed into two first order integrals using integration by parts as outlined by Hering [19] to yield

$$\theta(Z) = 1 + N\int_0^Z (Z - \tau)\left[\theta^4(\tau) - B^*_R(\tau)\right] d\tau - \int_0^1 Z\left[\theta^4(\tau) - B^*_R(\tau)\right] d\tau . \tag{II-40}$$

The above equation could be readily solved by numerical techniques if $B_R^*(\tau)$ were known.

The procedure outlined by Sparrow and Cess [26] was used to determine $B_R^*(\tau)$. The rod and base were considered to be M isothermal elements. When the ith element was considered, the integral equation (II-35) for $B_R^*(\tau)$ was expressed as a summation

$$B_i^* = \epsilon_i \theta_i^4 + \rho'_i \sum_{j=1}^{j=M} B_j^* F_{\delta A_i - \delta A_j} \qquad \text{(II-41)}$$

where $1 \leq i \leq M$. Equation (II-41) was rewritten as

$$\sum_{j=1}^{j=M} X_{ij} B_i^* = \theta_i^4 \qquad \text{(II-42)}$$

where

$$X_{ij} = \frac{\delta_{ij} - (1 - \epsilon_i) F_{\delta A_i - \delta A_j}}{\epsilon_i} \quad . \qquad \text{(II-43)}$$

The term δ_{ij} is the Kronecker delta which is 1 when $i = j$, and zero when $i \neq j$. The coefficients, X_{ij}, of equation (II-42) form an M- by -M matrix where $1 \leq i \leq M$ and $1 \leq j \leq M$

$$X = \begin{vmatrix} X_{11} & X_{12} & \cdots & X_{1M} \\ X_{21} & X_{22} & \cdots & X_{2M} \\ \cdot & \cdot & & \cdot \\ \cdot & \cdot & & \cdot \\ \cdot & \cdot & & \cdot \\ X_{M1} & X_{M2} & \cdots & X_{MM} \end{vmatrix} \qquad \text{(II-44)}$$

The inverse matrix of X was defined as ψ,

$$\psi = \begin{vmatrix} \psi_{11} & \psi_{12} & \cdots\cdots & \psi_{1M} \\ \psi_{21} & \psi_{22} & \cdots\cdots & \psi_{2M} \\ \cdot & \cdot & & \cdot \\ \cdot & \cdot & & \cdot \\ \cdot & \cdot & & \cdot \\ \psi_{M1} & \psi_{M2} & \cdots\cdots & \psi_{MM} \end{vmatrix} \quad . \tag{II-45}$$

The coefficients, ψ_{ij}, were used and equation (II-42) was rewritten as

$$B_i^* = \sum_{j=1}^{j=M}{}' \psi_{ij}\, \theta_j^4 \quad . \tag{II-46}$$

The above equation was used to determine $B_R^*(\tau)$ of equation (II-40). The specimen was broken into 11 isothermal elements along the rod and 9 on the base surface. This technique for determining $B_R^*(\tau)$ allowed equation (II-40) to be numerically integrated to yield the temperature distribution along the rod.

No attempt was made herein to elaborate the above technique for calculating B_i^*, and only the steps needed to complete the computer program were presented.

Equation (II-40) was numerically integrated using the trapezoidal rule where the rod was broken into 11 segments and the base, 9. An initial value of $\theta = 1$ was assumed to calculate B_i^*. Then B_i^* was used to calculate a θ value which was used as a second input. The process was repeated until agreement was reached.

Since this solution did not directly yield the value for $\left(\frac{d\theta}{dZ}\right)_{Z=1}$, as did the Runge-Kutta solution for the black case, the heat transfer was calculated by determining the slope at Z=0 using the following numerical differentiation formula [27]:

$$\left(\frac{d\theta}{dZ}\right)_{Z=1} = \frac{1}{12\,\Delta Z}\,(-3\theta_4 + 16\theta_3 - 36\theta_2 + 48\theta_1 - 25\theta_0) \qquad \text{(II-47)}$$

The subscripts refer to the beginning points of the first five isothermal elements of the rod. By using this value for $\left(\frac{d\theta}{dZ}\right)_{Z=0}$, the rod heat transfer was determined as before, using equation (II-21).

EXPERIMENTAL INVESTIGATION

The experimental setup consisted of the test specimen, the high altitude simulation system, and the data acquisition system as illustrated in Figure C-3 of Appendix C. A detailed description of the high altitude simulation system and the data acquisition system is presented in Appendix B.

The test specimen consisted of two prime parts — the 2.54-cm (1-inch) diameter aluminum rod and the flat circular 20.32-cm (8-inch) diameter aluminum base. Both the base and the rod had individual heating elements. The base was designed in two halves so that it could be mounted on the rod without disturbing the heater and the thermocouples previously used to determine the temperature distribution of the rod alone.

Base

The base surface consisted of two halves of a circular plate (mounting attachments so that the base could be fixed to the rod), a heater element on each half, and 12 thermocouples spot-welded to the base surface viewing the fin as shown in Figure C-2. Three different heater arrangements were bench tested before a satisfactory temperature distribution was obtained. The configuration selected was one with heater wires closely spaced in a circular pattern.

The base heater was constructed in the following manner. Two heater wire terminal posts were affixed to each half of the base and the surface was then covered with a layer of fiberglass tape to electrically insulate the heater wire and base surface. Then 16-gauge Chromel-A resistance wire with a resistance of 0.830 ohms per meter (0.253 ohms per foot) was wound circumferentially on each half of the base. The heater wire was covered by a layer of asbestos (0.318 cm thick); this was held in place by a piece of aluminum sheet stock (0.079 cm thick) attached to the base by screws. The resistances of the base surface heaters were measured and found to be 5 ohms each.

For bench testing the base specimen heaters were connected to a 30-volt, 10-amp, DC power supply. The current to the heater wire was controlled by a variable resistance. The thermocouple cold junction reference was an ice bath and the thermocouple millivolt output was recorded on a strip

chart by a Brown-Marco recording system. Several tests were conducted at different power levels and the base temperature spread was determined after steady state was reached. Steady state was normally achieved in about three-fourths of an hour. The tests were conducted at room temperature of approximately 297.6° K (76° F).

The base heater configuration selected produced a maximum temperature differential of 8° F at an average surface temperature of 388.7° K (240° F). This was considered acceptable since the temperature distribution was expected to be much more uniform in vacuum.

Fin

The rod or fin portion of the test specimen consisted of an aluminum alloy rod, a heater element, and 48 thermocouples as shown in Figure C-1. The rod specimen was a 2.54-cm (1-inch) diameter 6061 T6 aluminum alloy rod approximately 60.96 cm (24 inches) long. One end of the rod was circumferentially wound for approximately 10.16 cm (4 inches) with a heater wire; the remainder of the rod contained 48 thermocouples evenly spaced at 12 stations; the end of the rod opposite the heater had 4 thermocouples spot-welded to the end which was covered with one-fourth inch of insulation. The 48 thermocouples were located at intervals of 4.45 cm ($1\frac{3}{4}$ inches) with 4 couples at each station. The 4 thermocouples at each station were evenly spaced around the circumference of the rod.

The fin heater was constructed in the following manner. First, the rod

was wrapped with a layer of fiberglass tape to electrically insulate the heater wire from the rod. The heater wire was then attached to one terminal post and wound around the rod and attached to the second terminal post. It was then coated with a layer of Ceramacoat 512 (AREMCO Products, Inc., Briarcliff Manor, New York) and wrapped with a 1.27-cm (1/2-inch) layer of asbestos cloth. The heater resistance was measured and found to be 1.16 ohms.

The power input to the rod and also to the base was a closely regulated DC power supply. Variable resistances were placed in both base and rod power leads so that the desired power supply could be accurately achieved. The power input was determined by two Hewlett-Packard model 3430A digital voltmeters. One measured the system voltage drop and the other measured the voltage across a known resistance placed in one leg of the circuit.

Test Setup

The test specimen was suspended in the vacuum chamber by a cord at either end of the specimen which attached to a horizontal cross member as shown in Figure C-1. The test specimen thermocouple leads were taped to the supporting cross member and then fed through the chamber wall with a standard vacuum feedthrough connector. A thermocouple cold junction, ice bath, was located adjacent to the chamber and then the thermocouples were connected with the data acquisition system. The test specimen power leads were similarly fed through the vacuum chamber wall and connected to the regulated DC power source. Separate vacuum feedthrough connectors were used for the power leads and thermocouples to avoid any interference.

The vacuum chamber walls were painted black to minimize the reflected energy. To prevent the complications of having to account for an incident energy distribution on the specimen, the vacuum chamber wall was maintained at 78.7° K (-318° F) by circulating liquid nitrogen through the vacuum chamber wall. The temperature distribution of the rod without the base was solved numerically, including the sink temperature of 78.7° K to verify that the incident energy was negligible. The inclusion of the incident energy was calculated to produce less than 0.1% change in the temperature at the end of the rod.

Experimental Procedure

The test was designed to explore the temperature range from ambient to approximately 533° K (500° F). Based on the eariler rod tests by Shouman, approximate values of the rod temperature were known for various power inputs to the rod heater. Also, it was known that approximately 8 hours were required to achieve steady state heat transfer. Seven of the 20 test runs were conducted on a single 8-hour shift. For these runs the rod and base power supplies were left on overnight to permit faster achievement of steady state conditions. Steady state was considered achieved when all temperatures on the rod varied less than 1 degree per hour. This assumption was well borne out by longer runs that permitted a steady state condition where essentially no temperature variations were noticeable.

The test runs are summarized in Tables C-2 and C-3 of Appendix C. Test runs 1 through 7 were conducted with the base installed. Test runs 8, 9, and 10 were conducted with the rod only, and runs 11, 12, and 13 were conducted with the rod only and a smoke black carbon coating. Test runs 14 through 17 were conducted with the base installed and both the base and the rod carbon coated. Test runs 18, 19, and 20 were a repeat of run 12 to study the effect of removing the thermocouples. All test runs, except the first one, were made with liquid nitrogen cooling the chamber walls.

The initial test was conducted without liquid nitrogen and without power to the base to observe the effect of the presence of the base. This was an abbreviated test run and the thermal equilibrium was questionable. Test 2 was a repeat of test 1 but with liquid nitrogen in the cooling jacket.

Since the test specimen had individual heaters on the rod and base, it was highly impractical from a time standpoint to achieve equal temperatures on the base and the fin at the base fin intersection. Because of this problem the tests with the base were planned to achieve a somewhat higher and a somewhat lower temperature than the fin temperature at the base. Test 3 and test 4 satisfied this requirement for the initial power setting to the rod. For tests 5, 6, and 7 the procedure for tests 2, 3, and 4 was repeated with a different power supply to the rod heater as shown in Table C-2 of Appendix C.

The base was removed and tests 8, 9, and 10 were conducted with three different power inputs to the rod heater. These data were desired so

that the case of base surface interaction could be compared to the rod only, without interactions.

A carbon black coating was applied to the rod and base to obtain data that would satisfy a black surface analysis. The coating was applied by holding an acetylene torch burning an acetylene rich mixture near the specimen and rotating it until a velvety black coating was obtained over the entire surface of the rod and base. Tests 11, 12, and 13 were then made using the rod only. These tests were similar to tests 8, 9, and 10. Tests 14, 15, 16, and 17 were then conducted with the base installed. The procedure was again to obtain data with the base temperature somewhat above and below the rod temperature.

Test runs 18, 19, and 20 were then conducted with the rod only to ascertain the effect of the thermocouples mounted on the rod. The power input for these tests was maintained the same as for test 12. For test 18, one-half of the thermocouples were removed leaving 2 thermocouples at each of 12 stations. For test 19, one-half of the remaining thermocouples were removed leaving 1 thermocouple at each station except the fifth station which had none. Test 20 was conducted with 1 thermocouple at the heater end and 1 at the insulated end of the rod.

The test procedure was essentially the same for all test runs once the specimen was prepared for that particular test. The test runs were begun by simultaneously turning on the data acquisition system, the power supply to the specimen heaters, the backing pump, the heaters to the ejector pump and diffusion pump, the cooling water to the pump condensers, and then pressurizing

the liquid nitrogen storage trailer (for test runs 1 through 7 the specimen heater power supply was turned on the previous day and left on all night). When the diffusion and ejector pump oil reached approximately 545°K (520°F), the roughing pump was turned on and the liquid nitrogen flow to the pumping system cold trap and to the vacuum chamber cooling jacket was begun. The vacuum was then read on the Pirani gauge and the system was switched to "hi-vacuum," or onto the diffusion and ejector pumps when the vacuum reached 150 microns.

After hi-vacuum operation was achieved, the procedure consisted of checking the vacuum, thermocouple ice bath, heater power supply readings, and the specimen temperature distribution periodically. The specimen temperature was observed until steady state was achieved and then a new test run was begun by changing the power inputs to the specimen. Once a test run or series of runs was completed all of the test equipment was turned off and the nitrogen storage trailer vented. The cooling water to the ejector and diffusion pump oil condenser was left on for approximately 2 hours to protect solder joints.

RESULTS

Test Cases

Twenty tests were conducted as described in the experimental chapter, and equations (II-18) and (II-40) were solved (using the rod temperature at the base location as the initial temperature value) to determine the correlation between the analytical predictions of the temperature distributions and the experimental data. The test and calculated temperature distributions were plotted in Figures C-4 through C-9 of Appendix C. Since the fin root temperature and base temperature values for the test cases were used as starting points for the analytical solutions, the error between the test data and the calculated temperatures was greatest at the end of the fin and was used as a criterion to determine agreement between the two. The test data agreement with the analytical predictions ranged from -2.34 % to +5.97 % as shown in Table C-4 of Appendix C.

By examination of the percentage error for each test as presented in Table C-4 of Appendix C, it was seen that the first 10 tests showed a smaller error than the last 10 and that the error for the first 10 tests was negative and was positive for the last 10. The first 10 tests were conducted with the specimen uncoated and the last 10 tests were conducted with the specimen coated. Also it was shown by tests 12, 18, 19, and 20 (Figures C-8 and C-9

of Appendix C) that the presence of the thermocouples affected the temperature distribution. The coating effect and the thermocouple effect were then investigated further.

The thermocouple effect was experimentally investigated in the last 3 test runs by maintaining the power input to the rod constant at the value used in test 12. The thermocouples were progressively removed as described in the experimental chapter. Examination of the temperature distribution curves of Figures C-8 and C-9 of Appendix C showed that the rod temperature was forced higher to dissipate the constant heat input when the thermocouples were removed. The fin temperature increased approximately 6.7°K (12°R) at the root of the fin and approximately 3.9°K (7°R) at the insulated end when the 48 thermocouples were reduced to only 1 thermocouple at each end of the rod.

The heat transfer was then calculated from equation (II-21) using the slope that was determined by the numerical solution of equation (II-18). The calculated heat transfer showed a progressive increase with the removal of the thermocouples even though the heat input to the specimen was constant. This was expected since the math model did not compensate for the thermocouple and an increase in the rod base temperature would result in a greater calculated initial slope. This indicated increase in heat transfer was attributed directly to the thermocouples. The heat transfer from the rod for

the thermocouple correction test cases based on the calculated temperature distributions was:

Test	q_R (W)	q_R (Btu/hr)
12	19.77	67.5
18	21.47	73.3
19	22.00	75.1
20	22.14	75.6

These results showed that a 10.7 % change in heat transfer resulted from the presence of the thermocouples.

The test data were then used to determine the heat transfer for the thermocouple test runs. The initial slopes for test runs 12, 18, and 19 were determined by the numerical differentiation formula (II-47). Even though the heat input was constant to the rod, the slope was expected to vary for each test since the heat loss at each thermocouple station would decrease as the thermocouples were removed. Equation (II-21) was then used to calculate the heat transfer from the rod which was:

Test	q_R (W)	q_R (Btu/hr)
12	13.36	45.6
18	14.85	50.7
19	15.52	53.0

The heat transfer for test 20 was not presented because only two data points were taken which were not enough to determine the slope. These results showed that a 14 % change in heat transfer resulted from the presence of the thermocouples.

The percentage of heat transfer attributed to the thermocouples by the above methods showed relatively good agreement while the heat transfer

showed a wide disparity. The heat transfer based on the test data was considerably lower than that based on the analytical solution, and as noted before the temperature error went from negative to positive and increased in magnitude when the surface coating was added. Based on these results, the coating used on the last 10 test runs apparently induced more error (and in the opposite direction) than the thermocouples. Further quantitative analysis of the thermocouple effect did not appear meaningful because of the coating effect and because the heat transfer from the rod cannot be precisely determined. The heat input to the specimen was precisely measured but it could not be accurately determined what amount of heat was lost from the rod and what amount was lost from the heater portion of the test specimen.

The specimen was coated after the thermocouples were installed and therefore the layer of coating actually insulated the surface of the rod and the thermocouples. Consequently, the thermocouples were reading the rod surface temperature and therefore indicated a temperature higher than the surface temperature of the coating. To study this effect, test 19 was used because it had the fewest number of thermocouples and yet provided a data point at each station. The following numerical differentiation formulae [27] were used to calculate the slope of the temperature distribution at each station location:

$$\left(\frac{d\theta}{dZ}\right)_0 \approx \frac{1}{12\Delta Z}\left[-\theta_2 + 8\theta_1 - 8\theta_{-1} + \theta_{-2}\right] \qquad \text{(IV-1)}$$

$$\left(\frac{d\theta}{dZ}\right)_1 \approx \frac{1}{12\Delta Z}\left[3\theta_2 + 10\theta_1 - 18\theta_0 + 6\theta_{-1} - \theta_{-2}\right] \qquad \text{(IV-2)}$$

$$\left(\frac{d\theta}{dZ}\right)_{-1} \approx \frac{1}{12\Delta Z}\left[\theta_2 - 6\theta_1 + 18\theta_0 - 10\theta_{-1} - 3\theta_{-2}\right] \qquad \text{(IV-3)}$$

$$\left(\frac{d\theta}{dZ}\right)_{2} \approx \frac{1}{12\Delta Z}\left[25\theta_2 - 48\theta_1 + 36\theta_0 - 16\theta_{-1} + 3\theta_{-2}\right] \qquad \text{(IV-4)}$$

$$\left(\frac{d\theta}{dZ}\right)_{-2} \approx \frac{1}{12\Delta Z}\left[-3\theta_2 + 16\theta_1 - 36\theta_0 + 48\theta_{-1} - 25\theta_{-2}\right] \qquad \text{(IV-5)}$$

Equation (IV-1) was used to find the slope of the curve 3 or more data points away from either end of the curve. Equations (IV-3) and (IV-5) were used for the 2 points at the beginning of the curve, and equations (IV-2) and (IV-4) were used for the 2 points at the end of the curve. The negative subscripts denote stations left of zero and the positive subscripts denote stations to the right of zero.

The heat flowing through the rod by conduction at each station was then calculated from Fourier's law using the slopes calculated at each station. The heat lost by radiation for the rod sections between stations was the difference between the heat conducted into the section at the first station and the heat conducted out at the next station. This method determined that the first section of the rod lost 3.0 W (10.2 Btu/hr) and each of the remaining sections lost approximately 1.3 W (4.3 Btu/hr).

The temperature drop across the layer of coating was then calculated from Fourier's law assuming that the rod section was iosthermal in the longitudinal direction. The carbon black coating was assumed to be 0.025 cm (0.010 inch) thick and the thermal conductivity value was taken from a table in reference 1 which presented data for lamp soot at low pressure. These calculations indicated an 18.4°K (33.2°R) temperature drop across the coating

on the first section and approximately 7.8°K (14°R) across the coating on the remaining sections.

A corrected temperature distribution was then computed from equation (II-18) using an initial temperature equal to the indicated test temperature minus 18.4°K (33.2°R) or 333.0°K (599.37°R). This curve was plotted in Figure C-9 of Appendix C and designated θ_c. The test data disagreement was reduced from 4.9 % to 3.2 % based on the end point temperature. Although this did not explain the error in the data, it did indicate a trend in the proper direction to explain the positive error for each case where the coating was applied. Other variables which could not be accurately determined were the actual thickness and the thermal conductivity of the coating. Also, the coating was of a porous nature with a velvety surface composed of many small peaks and valleys which would radiate from some point beneath the actual surface. This compounded the problem of determining the coating thickness.

Parameter Study

In addition to the analytical predictions of the test cases, several temperature distributions were calculated using equation (II-18) by varying the governing dimensionless parameters. The black case was the only one considered since for efficient heat transfer the surface would be made as black as possible. The configuration factor $F_{dA_R - A_B}$ was plotted versus the length of the rod, in Figure C-10 of Appendix C, for the test specimen case to visualize how it affected the temperature distribution equation (II-18)

$$\frac{d^2\theta}{dZ^2} = N_c \left[\theta^4 - F^*_{\delta A_R - A_B}\right]$$

where $\theta_B = 1$.

The above equation was then solved for values of N_c of 0.5, 2, and 10. The dimensionless ratios, R_1 and R_2, which appeared in the term $F_{dA_R - A_B}$ were varied over a wide range. The limiting cases of no base and an infinite base were also solved for each value of N_c. The resulting temperature distributions were plotted in Figures C-11, C-12, and C-13 of Appendix C.

Some interesting limiting cases of the temperature distribution were plotted in Figure C-14. The case of infinite conductivity yields a uniform temperature along the rod equal to the base temperature. For the case of zero conductivity the governing equation for the temperature of a differential element of the rod viewing the base from a distance Z, reduces to

$$\theta(Z) = \left[F_{dA_R - A_B}\right]^{1/4} \qquad \text{(IV-6)}$$

For a base with an infinite radius ($R_2 = \infty$), $F_{dA_R - A_B} = 0.5$ and the temperature along the rod is constant at $\theta = (0.5)^{1/4}$ or 0.8409. Three other limiting cases for zero conductivity were also presented in Figure C-14 of Appendix C.

The dimensionless heat transfer or fin efficiency was calculated from equation (II-21) for each of the calculated temperature distributions. The fin efficiency was plotted versus the conduction parameter for the limiting cases of $R_2 = R_1$ (no base), $R_2 = \infty$ (infinite base, $F_{dA_R - A_B} = 0.5$) and

two intermediate values of R_2 for each value of R_1. The results are presented in Appendix C in Figures C-15, C-16, C-17, C-18, and C-19. From these curves it is seen that a low value of N_c is required to maintain a high efficiency. Also it was observed that the fin efficiency for values of $N_c > 0.05$ was decreased by approximately 50 % from the no base condition to an infinite base for all values of R_1 considered.

The temperature distribution curves and efficiency curves are applicable to gray surfaces if only singly reflected radiation rays are considered. It is only necessary to change the N_c to N'_c where $N'_c = \epsilon N_c$.

CONCLUSIONS

The experimental data and the numerical solutions showed reasonable trend agreement. The experimental data, however, were substantially affected by two identified sources of error:

1. the heat conducted from the rod by the thermocouples
2. the insulation effect of the carbon coating covering the rod surface and the thermocouple junction.

The above mentioned errors would tend to invalidate the assumption of one-dimensional heat transfer. Also the fact that the thermal properties of the specimen material were assumed constant would induce some error since ϵ and k would vary somewhat with temperature. The emissivity could vary with

time from test to test since some surface oxidation would occur. As a result of these errors the data did not agree with the analytical predictions as closely as was desirable for use in quantitative predictions. The trends did agree, however, and the data were within the range of the identified errors in the experiment.

The calculated temperature distributions for a given value of the conduction parameter were bounded by the cases of no base, and an infinite base; the temperature spread between the two cases increased with increasing N_c. The temperature distribution traversed the range between the limiting cases as the values of R_1 and R_2 were varied such that the configuration factor between the rod and the base varied from 0 to 0.5.

The heat transfer from a rod or the rod efficiency may vary a large amount with changing base size. The variation may be as much as approximately 50% for values of $N_c \geq 0.05$.

George C. Marshall Space Flight Center
National Aeronautics and Space Administration
Marshall Space Flight Center, Alabama 35812, July 1968
124-09-05-00-62

APPENDIX A.

CONFIGURATION FACTOR ANALYSIS

Configuration Factor $F^{*}_{\delta A_R - A_B}$

The configuration factor $F_{\delta A_R - A_B}$ of equation (II-18) was determined by the contour integral method [26]. The basic equation for the configuration factor for an infinitesimal element on the rod to that portion of the base which it views is

$$F_{dA_R - A'_B} = \int_{A'_B} \frac{\cos \varphi_B \cos \varphi_R}{\pi S^2} = \int_{A'_B} f(\varphi_B, \varphi_R \bar{S})\, dA'_B \,. \qquad \text{(A-1)}$$

Applying Stokes theorem to the above area integral results in the following contour integral

$$\begin{aligned} F_{dA_R - A'_B} = l_R \oint & \frac{(z_B - z_R)\,dy_B - (y_B - y_R)\,dz_B}{2\pi S^2} \\ + m_R \oint & \frac{(x_B - x_R)\,dz_B - (z_B - z_R)\,dx_B}{2\pi S^2} \\ + n_R \oint & \frac{(y_B - y_R)\,dx_B - (x_B - x_R)\,dy_B}{2\pi S^2} \end{aligned} \qquad \text{(A-2)}$$

where l_R, m_R, n_R are direction cosines of the normal to the surface dA_R, and the cosine of the angles, φ_B and φ_R, between the normals and the

vector $\hat{S}$, connecting the differential areas has been written as the scalar products of $\hat{n}_R \cdot \hat{S}_{RB}$ and $\hat{n}_B \cdot \hat{S}_{BR}$. The contour integral equation was simplified by orienting the coordinate axes so that the normal to dA_R lies along the x axes, as shown in Figure A-1. Then by inspection, it was seen that $l_R = 1$ and $m_R = n_R = 0$; also $x_R = r_R$, $y_R = z_R = 0$, $z_B = c$ and $dz_B = 0$. The distance S between an infinitesimal area dA_R and dA_B was

$$S = \sqrt{(x_R - r_R)^2 + y_B^2 + z_B^2} \tag{A-3}$$

and the contour integral equation (A-2) reduced to

$$F_{dA_R - A'_B} = \oint_{A'_B} \frac{z_B \, dy_B}{2\pi[(x_R - r_R)^2 + y_B^2 + z_B^2]} \quad . \tag{A-4}$$

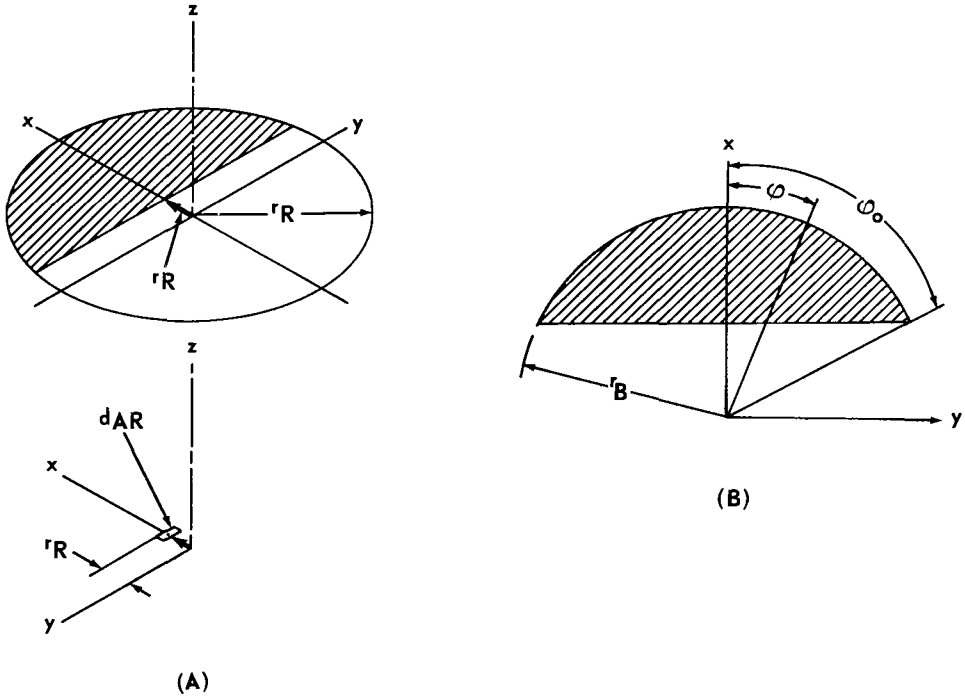

FIGURE A-1. BASE SURFACE AREA VIEWED BY DIFFERENTIAL ELEMENT ON ROD

The contour that bounded the area A'_B was composed of two parts as shown in Figure A-1B: an arc running from $-\varphi_0 \leq \varphi \leq \varphi_0$ and a straight line running from $-r_B \sin\varphi_0 \leq y_B \leq r_B \sin\varphi_0$. On the arc $x_B = r_B \cos\varphi$ and $y_B = r_B \sin\varphi$; whereas on the striaght line $x_B = r_B \cos\varphi_0$, and $dx_B = 0$. When equation (A-4) was integrated along the arc and then along the straight line of Figure A-1. B, it became

$$F_{dA_R - A'_B} = \frac{z_B}{\pi} \int_{\varphi_0}^{0} \frac{r_B \cos\varphi \, d\varphi}{r_B^2 + r_R^2 + z_B^2 - 2r_R r_B \cos\varphi} + \frac{z_B}{\pi} \int_{-r_B \sin\varphi_0}^{0} \frac{dy_B}{(r_B \cos\varphi_0 - r_R)^2 + y_B^2 + z_B^2} \qquad \text{(A-5)}$$

When $\sin\varphi_0$ and $\cos\varphi_0$ were written as

$$\sin\varphi_0 = \frac{r_B^2 - r_R^2}{r_B} \quad , \quad \cos\varphi_0 = \frac{r_R}{r_B} \, ,$$

and $r_B^2 + r_R^2 + z_B^2 = C$ and $-2r_R r_B = D$, equation (A-5) then became

$$F_{dA_R - A'_B} = \frac{z_B r_B}{\pi} \int_{\varphi_0}^{0} \frac{\cos d\varphi}{C + D\cos\varphi} + \frac{z_B}{\pi} \int_{-\sqrt{r_B^2 - r_R^2}}^{0} \frac{dy_B}{y_B^2 + z_B^2} \qquad \text{(A-6)}$$

Integration of equation (A-6) and substitution of limits yielded

$$F_{dA_R - A'_B} = \frac{1}{\pi} \tan^{-1}\left[\frac{\sqrt{r_B^2 - r_R^2}}{z_B}\right] + \frac{2z_B C r_B}{\pi D \sqrt{C^2 - D^2}} \tan^{-1}\left[\frac{(C - D)\tan\left(\frac{\varphi}{2}\right)}{C^2 - D^2}\right] - \frac{z_B r_B \varphi_0}{\pi D} \, . \qquad \text{(A-7)}$$

The term $\tan\left(\frac{\varphi_0}{2}\right)$ was expressed as

$$\tan\left(\frac{\varphi_0}{2}\right) = \frac{\sin\varphi_0}{1+\cos\varphi_0} = \frac{\sqrt{r_B^2 - r_R^2}}{r_B - r_R} \tag{A-8}$$

and substituted into equation (A-7). When the appropriate substitutions were made for C and D and when φ_0 was written as $\tan^{-1}$, the expression for the configuration factor became

$$F_{dA_R - A'_B} = \frac{1}{\pi}\tan^{-1}\left\{\frac{r_B^2 - r_R^2}{z_B}\right\} - \frac{z_B(r_B^2 + r_R^2 + z_B^2)}{\pi r_R\sqrt{(r_B^2 + r_R^2 + z_B^2)^2 - 4r_B^2 r_R^2}}$$
$$\tan^{-1}\left\{\frac{[(r_B + r_R)^2 + z_B^2]\sqrt{r_B^2 - r_R^2}}{(r_B + r_R)\sqrt{(r_B^2 + r_R^2 + z_B^2)^2 - 4r_B^2 r_R^2}}\right\}$$
$$+ \frac{z_B}{2\pi r_R}\tan^{-1}\left\{\frac{\sqrt{r_B^2 - r_R^2}}{r_R}\right\}. \tag{A-9}$$

When the above equation was nondimensionalized with respect to L, and R_1, R_2, and Z were defined as $R_1 = r_R/L$, $R_2 = r_B/L$, and $Z = z_B/L$, the nondimensional configuration factor became

$$F^*_{dA_R - A'_B} = \frac{1}{\pi}\tan^{-1}\left\{\frac{\sqrt{R_2^2 - R_1^2}}{z}\right\} - \frac{z(R_2^2 + R_1^2 + z^2)}{\pi R_1\sqrt{(R_2^2 + R_1^2 + z_B^2)^2 - 4R_2^2 R_1^2}}$$
$$\tan^{-1}\left\{\frac{[(R_2 + R_1)^2 + z^2]\sqrt{R_2^2 - R_1^2}}{(R_2 + R_1)\sqrt{(R_2^2 + R_1^2 + z^2)^2 - 4R_2^2 R_1^2}}\right\}$$
$$+ \frac{z}{2\pi R_1}\tan^{-1}\left\{\frac{R_2^2 - R_1^2}{R_1}\right\} \tag{A-10}$$

and from symmetry

$$F^{*}_{\delta A_R - A_B} = F^{*}_{dA_R - A'_B} \quad . \tag{A-11}$$

Configuration Factors $F_{\delta A_R - \delta A_B}$ and $F_{\delta A_B - \delta A_R}$

It was readily seen from the cylindrical symmetry of the specimen that the flux density at any arbitrary radius ρ on the base was constant for any arbitrary angle φ. The same was true for any φ position on the rod at a given z.

Now when a differential slice of the rod and a differential ring on the base were considered, it was seen that the radiosity distribution was uniform with the coordinate angle φ. However, the radiosity distribution varied along the length of the rod and also along any radius on the base.

Also from symmetry, the configuration factor from a differential element on the rod to the portion of a differential ring viewed on the base was equal to the configuration factor from the total differential ring around the rod to the total differential ring on the base, or

$$F_{dA_R - \delta A'_B} = F_{\delta A_R - \delta A_B} , \tag{A-12}$$

then

$$F_{dA_R - \delta A'_B} = \frac{1}{dA_R} \int_{\delta A'_B} f(\varphi_B, \varphi_R, \bar{S})\, dA_R\, dA_B , \tag{A-13}$$

or

$$F_{\delta A_R - \delta A_B} = \int_{\delta A'_B} f(\varphi_B, \varphi_R, \bar{S})\, dA_B \,. \qquad \text{(A-14)}$$

The differential areas were expressed as $dA_R = r_R dz d\varphi''$ and $dA_B = \rho d\rho d\varphi$, as shown in Figure A-2.

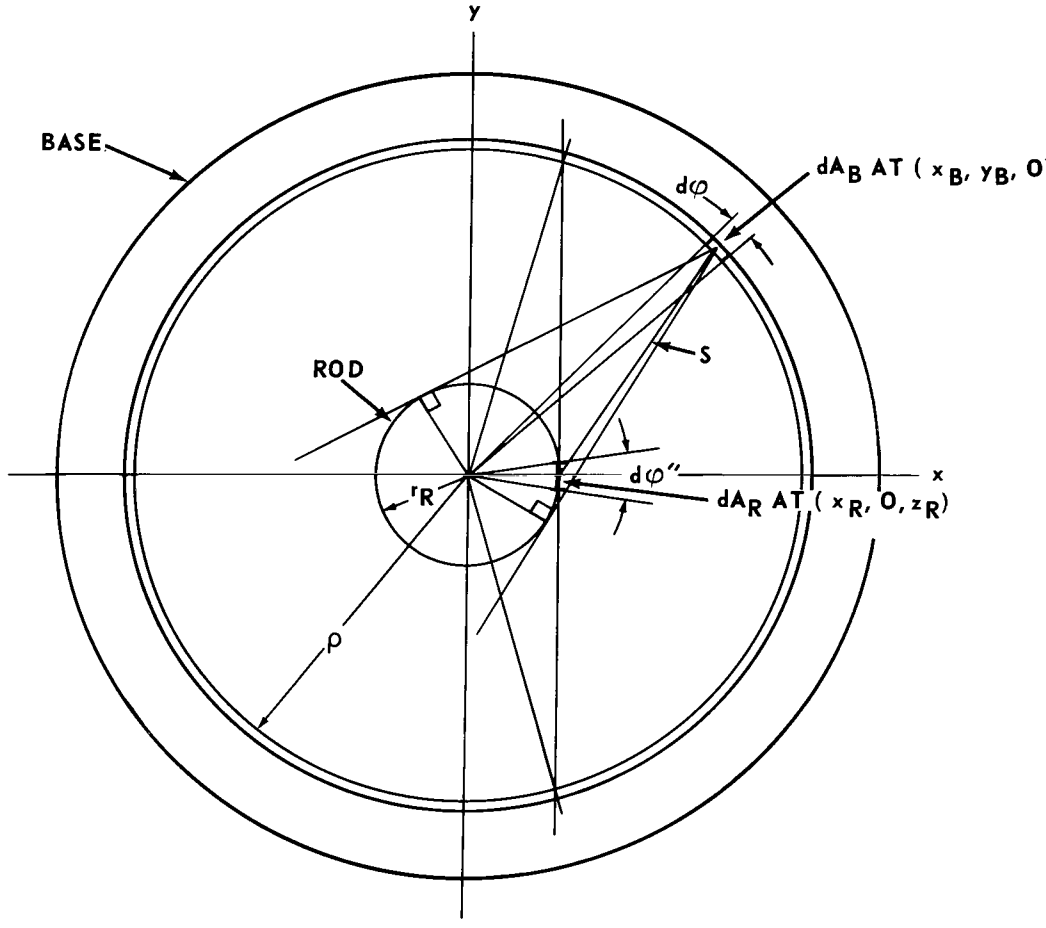

FIGURE A-2. COORDINATE ANGLE THROUGH WHICH EITHER dA_R CAN VIEW δA_B OR dA_B CAN VIEW δA_R

The total coordinate angle through which either differential element dA_R and dA_B could view the differential strips δA_B or δA_R was $2\cos^{-1} r_R/\rho$.

Therefore, the configuration factor from the differential strip δA_R to the differential strip δA_B could be written as 2 times the integral from 0 to $\cos^{-1}\frac{r_R}{\rho}$ or,

$$F_{\delta A_R - \delta A_B} = 2 \int_0^{\cos^{-1}\frac{r_R}{\rho}} f(\varphi_B, \varphi_R, \bar{S})\, dA_B \,. \qquad \text{(A-15)}$$

From the reciprocity relationship,

$$F_{\delta A_B - \delta A_R} = \frac{\delta A_R}{\delta A_B} F_{\delta A_R - \delta A_B}$$

$$= \frac{2\pi r_R dz}{2\pi \rho d\rho} F_{\delta A_R - \delta A_B}$$

$$F_{\delta A_B - \delta A_R} = \frac{r_R dz}{\rho d\rho} \left[2 \int_0^{\cos^{-1}\frac{r_R}{\rho}} f(\varphi_B, \varphi_R, S)\, dA_B \right] . \qquad \text{(A-16)}$$

The vector $\hat{S}$ was written as

$$\hat{S}_{RB} = (x - r_R)\,\hat{i} + y\hat{j} - z\hat{k} \qquad \text{(A-17)}$$

and

$$\hat{S}_{BR} = (r_R - x)\,\hat{i} - y\hat{j} + z\hat{k} \qquad \text{(A-18)}$$

and the magnitude of vector $\hat{S}$ was

$$S = \sqrt{(x - r_R)^2 + y^2 + z^2} \,. \qquad \text{(A-19)}$$

The normals to the rod and base areas were

$$\hat{n}_R = \hat{i} + (0)\hat{j} + (0)\hat{k} = \hat{i} \qquad \text{(A-20)}$$

$$\hat{n}_B = (0)\hat{i} + (0)\hat{j} + \hat{k} = \hat{k} . \qquad \text{(A-21)}$$

The cosines of the angle between the normals and the vector $\hat{S}$ were found by taking the vector dot product of the normal and the vector $\hat{S}$ and dividing by the product of the magnitude of $\hat{S}$ and the magnitude of the unit vector, which yielded

$$\cos \varphi_R = \frac{x - r_R}{\sqrt{(x - r_R)^2 + y^2 + z^2}} \qquad \text{(A-22)}$$

and

$$\cos \varphi_B = \frac{z}{\sqrt{(x - r_R)^2 + y^2 + z^2}} \qquad \text{(A-23)}$$

These were converted to cylindrical coordinates by substitution of $x = \rho\cos\varphi$ and $y = \rho\sin\varphi$ which yielded

$$\cos \varphi_R = \frac{\rho\cos\varphi - r_R}{\sqrt{\rho^2 + r_R^2 + z^2 - 2r_R \rho\cos\varphi}} \qquad \text{(A-24)}$$

$$\cos \varphi_B = \frac{z}{\sqrt{\rho^2 + r_R^2 + z^2 - 2r_R \rho\cos\varphi}} \qquad \text{(A-25)}$$

$$S^2 = \rho^2 + r_R^2 + z^2 - 2r_R \rho\cos\varphi . \qquad \text{(A-26)}$$

It was then written that

$$f(\varphi_B, \varphi_R, S) = \frac{(\rho\cos\varphi - r_R)(z)}{\pi(\rho^2 + r_R^2 + z^2 - 2r_R \rho\cos\varphi)^2} \qquad \text{(A-27)}$$

and substitution into equations (A-15) and (A-16) yielded

$$F_{\delta A_R - \delta A_B} = \frac{2z\rho d\rho}{\pi} \int_0^{\cos^{-1}\frac{r_R}{\rho}} \frac{(\rho\cos\varphi - r_R\rho)}{(\rho^2 + r_R^2 + z^2 - 2r_R\rho\cos\varphi)^2}\, d\varphi \tag{A-28}$$

and

$$F_{\delta A_B - \delta A_R} = \frac{2r_R z dz}{\pi} \int_0^{\cos^{-1}\frac{r_R}{\rho}} \frac{(\rho\cos\varphi - r_R)}{(\rho^2 + r_R^2 + z^2 - 2r_R\rho\cos\varphi)^2}\, d\varphi \tag{A-29}$$

When the integral in equations (A-28) and (A-29) was considered,

$$\int_0^{\cos^{-1}\frac{r_R}{\rho}} \frac{(\rho\cos\varphi - r_R)}{(\rho^2 + r_R^2 + z^2 - 2r_R\rho\cos\varphi)^2}\, d\varphi \ . \tag{A-30}$$

The integral (A-30) became

$$\int_0^{\cos^{-1}\frac{r_R}{\rho}} \frac{(\rho\cos\varphi - r_R)}{(a + b\cos\varphi)^2}\, d\varphi = \int_0^{\cos^{-1}\frac{r_R}{\rho}} \frac{A d\varphi}{(a + b\cos\varphi)^2} + \int_0^{\cos^{-1}} \frac{B d\varphi}{(a + b\cos\varphi)} \tag{A-31}$$

when a and b were defined as $a = \rho^2 + r_R^2 + z^2$ and $b = -2r_R\rho$ and the expression under the integral sign in equation (A-30) was separated, using partial fractions,

$$\frac{\rho\cos\varphi - r_R}{(a + b\cos\varphi)^2} = \frac{A}{(a + b\cos\varphi)^2} + \frac{B}{(a + b\cos\varphi)} \ , \tag{A-32}$$

where $B = \frac{\rho}{b}$ and $A = -\ r_R + \frac{\rho a}{b}$.

From the integral tables [28] the above integral was found to be

$$\int_0^{\cos^{-1}\frac{r_R}{\rho}} \frac{(\rho\cos\varphi - r_R)\,d\varphi}{(a + b\cos\varphi)^2} = \left\{ A \left[\frac{b \sin\varphi}{(b^2 - a^2)(a + b\cos\varphi)} - \frac{a}{b^2 - a^2} \left(\frac{2}{\sqrt{a^2 - b^2}} \tan^{-1} \frac{(a - b)\tan\left(\frac{\varphi}{2}\right)}{\sqrt{a^2 - b^2}} \right) \right] + \frac{2B}{\sqrt{a^2 - b^2}} \tan^{-1} \frac{(a - b)\tan\left(\frac{\varphi}{2}\right)}{\sqrt{a^2 - b^2}} \right\}_0^{\cos^{-1}\frac{r_R}{\rho}} \quad \text{(A-33)}$$

When the integration limits and the following relationships

$$\cos\varphi = \frac{r_R}{\rho}, \quad \sin\varphi = \frac{\sqrt{\rho^2 - r_R^2}}{\rho}, \quad \tan\left(\frac{\varphi}{2}\right) = \frac{\sin\varphi}{1 + \cos\varphi} = \frac{\sqrt{\rho^2 - r_R^2}}{\rho + r_R}$$

were substituted into equation (A-33) the expression became

$$\int_0^{\cos^{-1}\frac{r_R}{\rho}} \frac{(\rho\cos\varphi - r_R)\,d\varphi}{(a + b\cos\varphi)^2} = \frac{A\,b\sqrt{\rho^2 - r_R^2}}{\rho(b^2 - a^2)\left(a + b\frac{r_R}{\rho}\right)} - \frac{2aA}{(b^2 - a^2)\sqrt{a^2 - b^2}} \tan^{-1}\left[\frac{(a - b)\sqrt{\rho^2 - r_R^2}}{(\rho + r_R)\sqrt{a^2 - b^2}}\right] + \frac{2B}{\sqrt{a^2 - b^2}} \tan^{-1}\left[\frac{(a - b)\sqrt{\rho^2 - r_R^2}}{(\rho + r_R)\sqrt{a^2 - b^2}}\right] \quad \text{(A-34)}$$

and this was further simplified by substituting for A and B and combining terms to yield

$$\int_0^{\cos^{-1}\frac{r_R}{\rho}} \frac{(\rho\cos\varphi - r_R)\,d\varphi}{(a + b\cos\varphi)^2} = \frac{\sqrt{\rho^2 - r_R^2}}{a^2 - b^2}$$

$$- \frac{2(a\,r_R + \rho b)}{(a^2 - b^2)^{3/2}} \tan^{-1}\left[\frac{(a - b)\,(\rho - r_R)}{(a + b)\,(\rho + r_R)}\right]. \qquad \text{(A-35)}$$

When the above expression was used and appropriate substitutions were made for a and b, equation (A-28) for the configuration factor became

$$F_{\delta A_R - \delta A_B} = \frac{2z\rho d\rho}{\pi}\left\{\frac{\sqrt{\rho^2 - r_R^2}}{[(\rho^2 + r_R^2 + z^2)^2 - 4\rho^2 r_R^2]}\right.$$

$$+ \frac{2r_R(\rho^2 - r_R^2 - z^2)}{[(\rho^2 + r_R^2 + z^2)^2 - 4r_R^2\rho^2]^{3/2}}$$

$$\left.\tan^{-1}\left[\sqrt{\frac{(\rho^2 + r_R^2 + z^2 + 2r_R\rho)\,(\rho - r_R)}{(\rho^2 + r_R^2 + z^2 - 2r_R\rho)\,(\rho + r_R)}}\right]\right\} \qquad \text{(A-36)}$$

Similarly, equation (A-29) became

$$F_{\delta A_B - \delta A_R} = \frac{2r_R z dz}{\pi}\left\{\frac{\sqrt{\rho^2 - r_R^2}}{[(\rho^2 + r_R^2 + z^2) - 4\rho^2 r_R^2]}\right.$$

$$+ \frac{2r_R(\rho^2 - r_R^2 - z^2)}{[(\rho^2 + r_R^2 + z^2)^2 - 4r_R^2\rho^2]^{3/2}}$$

$$\left.\tan^{-1}\left[\sqrt{\frac{(\rho^2 + r_R^2 + z^2 + 2r_R\rho)\,(\rho - r_R)}{(\rho^2 + r_R^2 + z^2 - 2r_R\rho)\,(\rho + r_R)}}\right]\right\}. \qquad \text{(A-37)}$$

Equations (A-36) and (A-37) were expressed in the following form:

$$F^{*}_{\delta A_R - \delta A_B} = \frac{2ZRdR}{\pi} \left\{ \frac{\sqrt{R^2 - R_1^2}}{[(R^2 + R_1^2 + Z^2)^2 - 4RR_1]} \right.$$

$$+ \frac{2R_1(R^2 - R_1^2 - Z^2)}{[(R^2 + R_1^2 + Z^2)^2 - 4R_1^2R^2]^{3/2}} \qquad \text{(A-38)}$$

$$\left. \tan^{-1}\left[\sqrt{\frac{(R^2 + R_1^2 + Z^2 + 2R_1R)(R - R_1)}{(R^2 + R_1^2 + Z^2 - 2R_1R)(R + R_1)}} \right] \right\}$$

$$F^{*}_{\delta A_B - \delta A_R} = \frac{2R_1ZdZ}{\pi} \left\{ \frac{\sqrt{R^2 - R_1^2}}{[(R^2 + R_1^2 + Z^2)^2 - 4R^2R_1^2}} \right.$$

$$+ \frac{2R_1(R^2 - R_1^2 - Z^2)}{[(R^2 + R_1^2 + Z^2)^2 - 4R_1^2R^2]^{3/2}} \qquad \text{(A-39)}$$

$$\left. \tan^{-1}\left[\sqrt{\frac{(R^2 + R_1^2 + Z^2 + 2R_1R)(R - R_1)}{(R^2 + R_1^2 + Z^2 - 2R_1R)(R + R_1)}} \right] \right\}$$

when the dimensionless ratios $Z = z/L$, $R_1 = r_R/L$, $R = \rho/L$ were introduced.

APPENDIX B

EXPERIMENTAL EQUIPMENT

The experimental equipment consisted of the high altitude simulation system, the data acquisition system, and the emissivity measuring device. This equipment is government property maintained and operated by the Propulsion and Vehicle Engineering Laboratory of the George C. Marshall Space Flight Center.

High Altitude Simulation System

The high altitude simulation system or vacuum system consisted of the following primary components: vacuum chamber; diffusion pump, ejector pump, backing pump, and roughing pump; valves; pressure gauges; and liquid nitrogen storage trailer.

Vacuum Chamber. The vacuum chamber was a stainless steel cylinder approximately 1.83 m (6 feet) long and 1.22 m (4 feet) in diameter with a dished head at each end. One of the dished heads was hinged for a door and the other attached to the pumping system. The chamber environment was controlled by a cooling jacket which permitted a cooling liquid such as liquid nitrogen to be circulated through the cooling jacket and the chamber door. The door was a double wall construction connected to the jacket so that the cooling liquid circulated through both the jacket and the door. The interior surfaces of the

chamber that were viewed by the test specimen were painted black to minimize radiant energy reflections.

The vacuum chamber wall was designed with 3 ports that could be used for viewing or for instrumentation or for power feedthrough. For this test the ports were used for plugs to feedthrough 64 thermocouples and 2 power supplies.

Pumping System. The pumping system consisted of 4 pumps which could produce a vacuum chamber minimum pressure of 1×10^{-7} mm Hg. The chamber vacuum was initiated by a roughing pump of large capacity. After a rough vacuum was obtained (150 mm Hg), the low vacuum was achieved and maintained by a fractionating oil diffusion pump, an oil ejector pump, and a rotary backing pump operating in series. The pumping system was designed and manufactured by the Consolidated Electro-dynamics Corporation for NASA/MSFC. The following pumps were used in the system:

1. Type MCF-15000 fractionating oil diffusion pump with 0.81-m (32-inch) diameter casing.

   Operating Range: 5×10^{-7} to 5×10^{-4} mm Hg

   Maximum Speed: 899.9 m^3/min (31,779 cfm) at 3×10^{-4} mm Hg

2. Kinney Type KB-150 oil ejector pump.

   Operating Range: 6×10^{-4} to 4×10^{-1} mm Hg

   Maximum Speed: 11.53 m^3/min (407 cfm) at 3×10^{-2} mm Hg

3. Kinney Type KDH-130 rotary oil sealed backing pump.

   Free Air Displacement: 3.71 m^3/min (131 cfm) at 535 rpm

   Ultimate Pressure: 1×10^{-2} mm Hg

4. Kinney Type KD-310 rotary oil sealed roughing pump.

   Free Air Displacement: 8.81 m^3/min (311 cfm) at 360 rpm

   Ultimate Pressure: 1×10^{-2} mm Hg

Valves and Gauges. The high altitude simulation system design incorporated the necessary valves and pressure gauges to control the system. All system valves were hand operated except the 0.81-m (32-inch) valve between the vacuum chamber and the diffusion pump which was motor driven. There were 3 types of pressure gauges used in the system: a cold cathode ionization and a Pirani type were used to monitor the chamber vacuum; a Bourdon-tube gauge was used to monitor the pressure in the liquid nitrogen storage trailer. Both the high and low vacuum gauges were products of the Consolidated Vacuum Corporation, Rochester Division, Rochester, New York, and were of the following specifications:

1. Cold cathode ionization type

   Discharge Vacuum Gauge

   TYPE GPH-100A

   Three Range Selections from 25×10^{-3} to 1×10^{-8} millimeters of mercury

2. Pirani Vacuum Gauge

TYPE 2203-04

Two range selection 2000-50 microns

The Pirani gauge was used to monitor the vacuum while the system was operating at a low vacuum and the ionization gauge was used to monitor the vacuum when the system was operating at a high vacuum.

Liquid Nitrogen Storage Trailer. Liquid nitrogen was required for the vacuum pumping system cold trap and also for the vacuum chamber cooling jacket. The liquid nitrogen was supplied from an 8165.0-kg (9-ton) capacity liquid nitrogen storage trailer. The storage trailer was a self-pressurizing unit, and was maintained at a pressure of 1.72×10^5 - 2.07×10^5 N/m^2 (25-30 psig) for the test runs. Flow was controlled to the vacuum system by a hand valve and the storage trailer pressure was maintained by a hand vent valve and an automatic (spring-loaded) relief valve. The storage trailer was located outside of the building which houses the vacuum system for safety reasons, and the liquid nitrogen was supplied by a 2.54-cm (1-inch) diameter insulated pipe.

Data Acquisition System. The data acquisition system consisted of 64 thermocouples, a digital recording system, and a tape controlled typewriter.

The thermocouples were standard 30-gauge copper and constantan thermocouple wiring. The thermocouples were spot welded to the specimen and brought out of the vacuum chamber through a standard vacuum type feed-through electrical connector. A thermocouple cold junction (ice bath) was

located adjacent to the vacuum chamber and the thermocouple outputs were carried by way of a floor conduit to the recording system approximately 15.24 m (50 feet) away.

The digital recording system was a model ADRT 2100 manufactured by the Minneapolis-Honeywell Regulator Company. The system could record up to 100 channels of data. The system could successively sample and record data inputs at the rate of 100 points per minute through the use of stepping switches. A sampled input was amplified and then balanced against a precision voltage. The balance was obtained by successive approximation performed by relays pulling in successively decreasing increments of voltage. If an increment pulled in was too large, it was dropped and the next smaller increment pulled in; if the latter was too small, another smaller increment was pulled in, etc.,, until the balance was achieved. A digital output was then punched on paper tape along with the necessary control signals to control a Friden Flexowriter. The tape was fed through the Flexowriter control system at each recording interval and the data outputs were typed out in millivolt units. The data acquisition system could scan the selected number of inputs and punch the output values on paper tape once every 1/2, 1, 2, 5, 10, 20, 50, or 100 minutes, or continuously.

For this series of tests, 64 thermocouples were monitored and recorded at intervals of 5 minutes from test beginning to completion. All thermocouple millivolt outputs were available for individual call up at any time. In the call up mode, a digital reading appeared in lights by making the proper manual selection to read the particular measurement of interest.

The data acquisition system accuracy was dependent upon the range selected. For this test series a range of 0 to 10 millivolts was selected and the system accuracy in converting the thermocouple output was ±0.01 millivolts [approximately 0.22°K (0.4° F)].

Emissivity Measuring Device

The emissivity of the base surface specimen was measured by a Gier Dunkle-Emissivity Inspection System, Model EM 520, Geir Dunkle Instruments, Inc., Santa Monica, California. The emissivity inspection system measured the emittance of an opaque surface at room temperature. The system was composed of a heated radiometer connecting a flexible conduit to a carrying case containing the power supply. When a room temperature specimen surface covered the radiometer opening, the detector provided an output that was proportional to the infrared emittance of the specimen. The output was indicated on the self balancing potentiometer and this output was then converted to an emissivity valve. The emissivity measurement of the base surface specimen was made by personnel of Materials Division of Propulsion and Vehicle Engineering Laboratory and the emissivity was found to be 0.13.

APPENDIX C

ILLUSTRATIONS

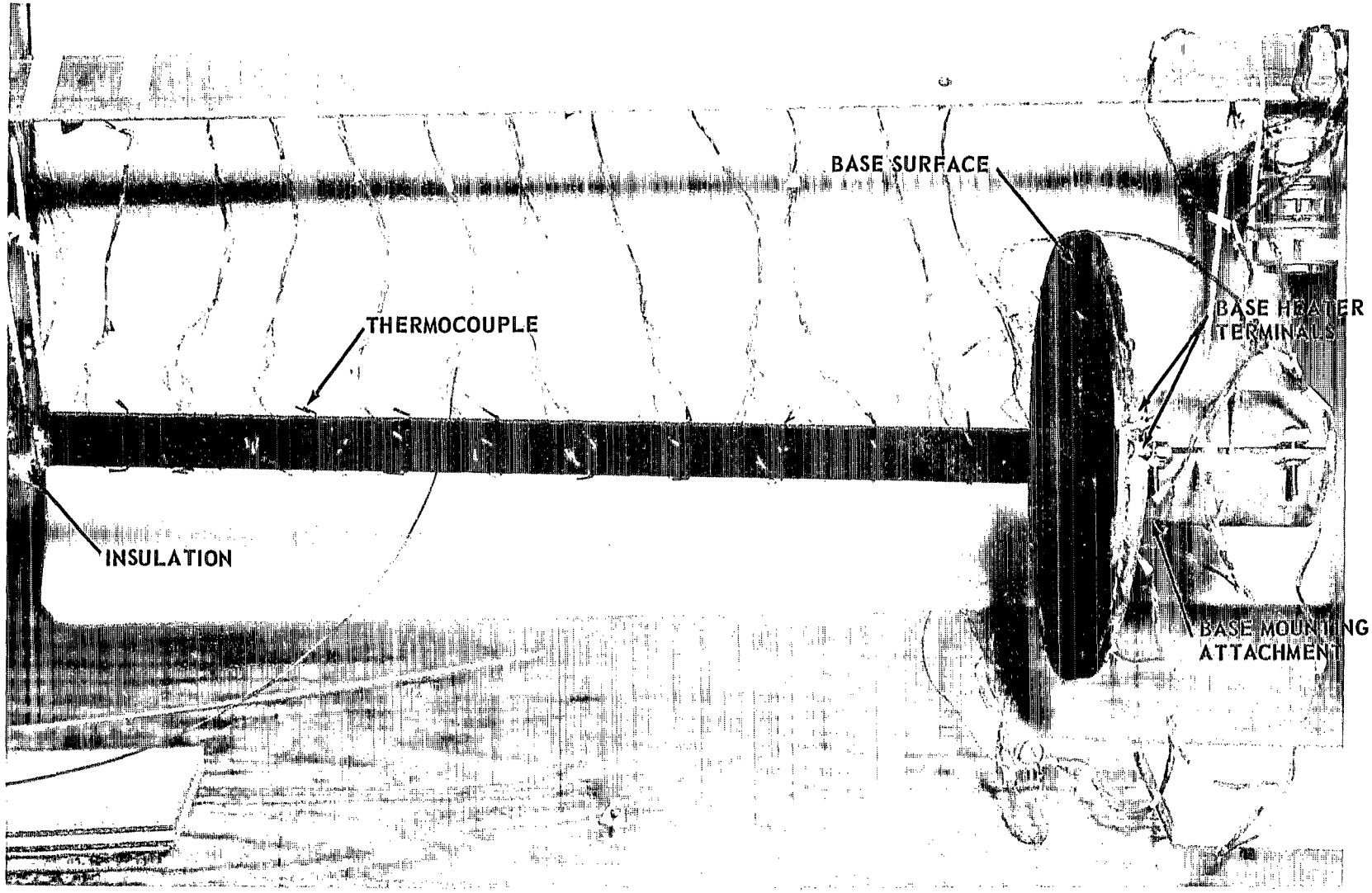

FIGURE C-2. TEST SPECIMEN (Specimen coated and base surface installed)

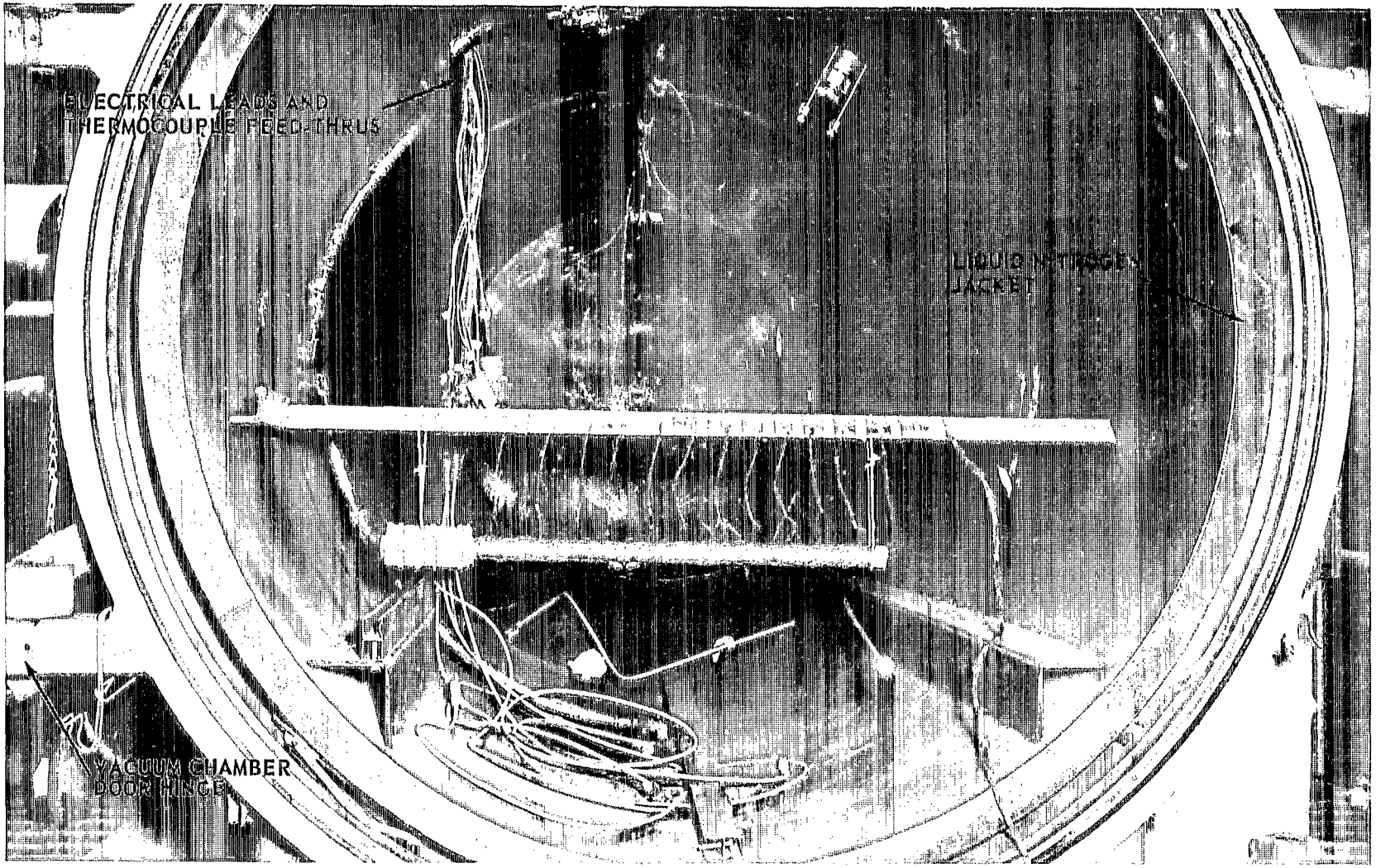

FIGURE C-1. TEST SPECIMEN MOUNTED IN VACUUM CHAMBER
(Specimen uncoated and base surface not installed)

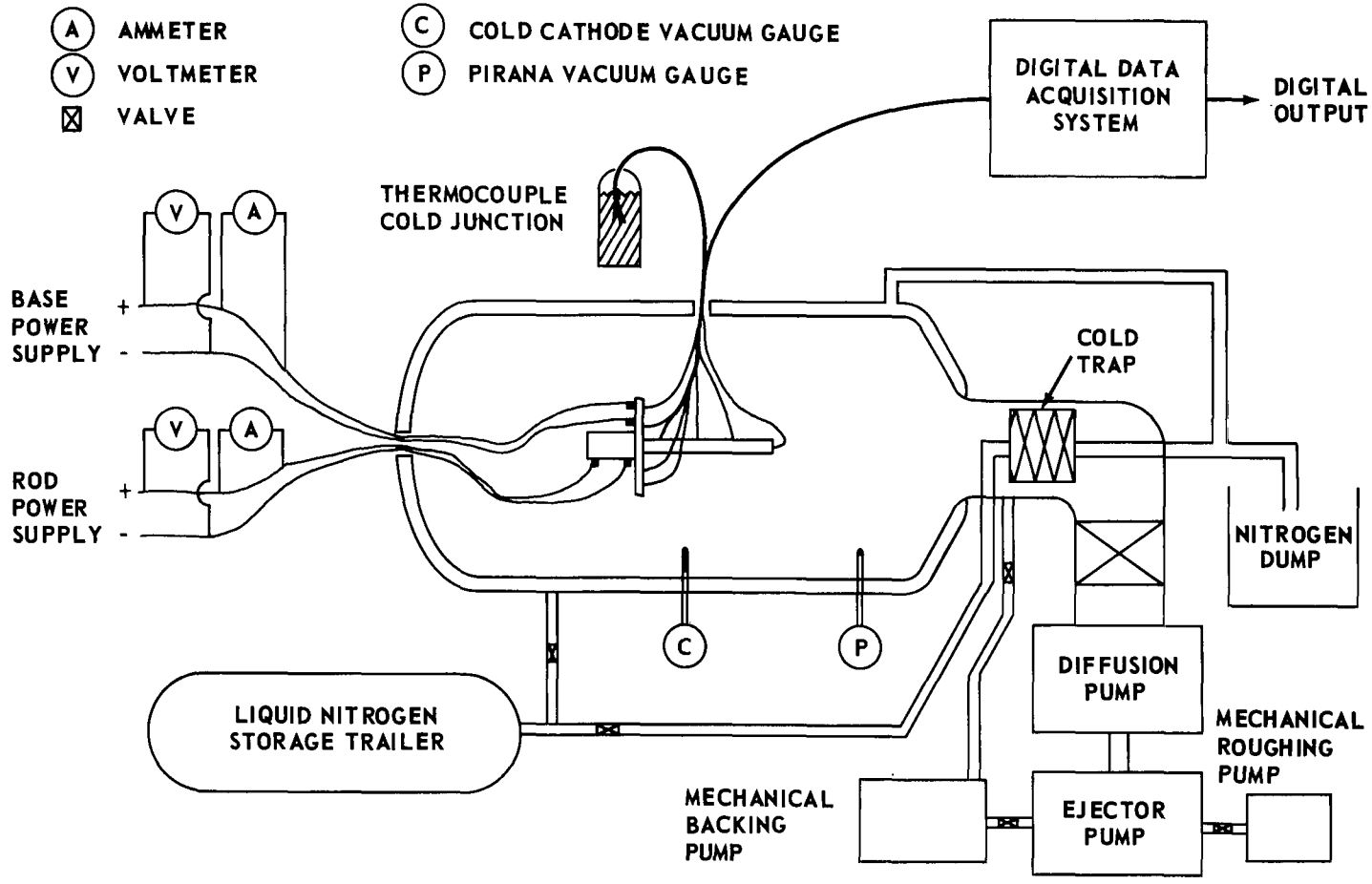

FIGURE C-3. SCHEMATIC OF TEST SETUP

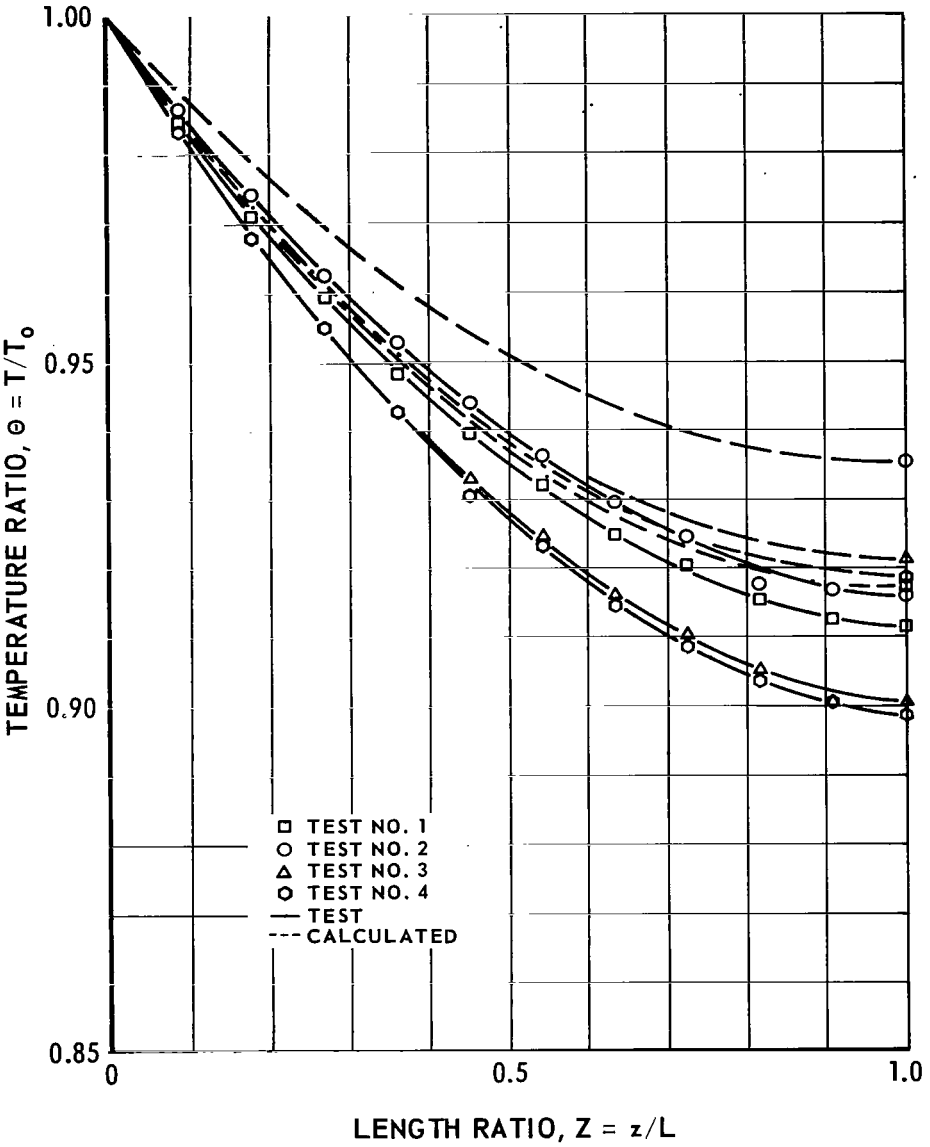

FIGURE C-4. TESTS 1-4 AND CALCULATED TEMPERATURE DISTRIBUTIONS FOR ROD WITH BASE (Uncoated)

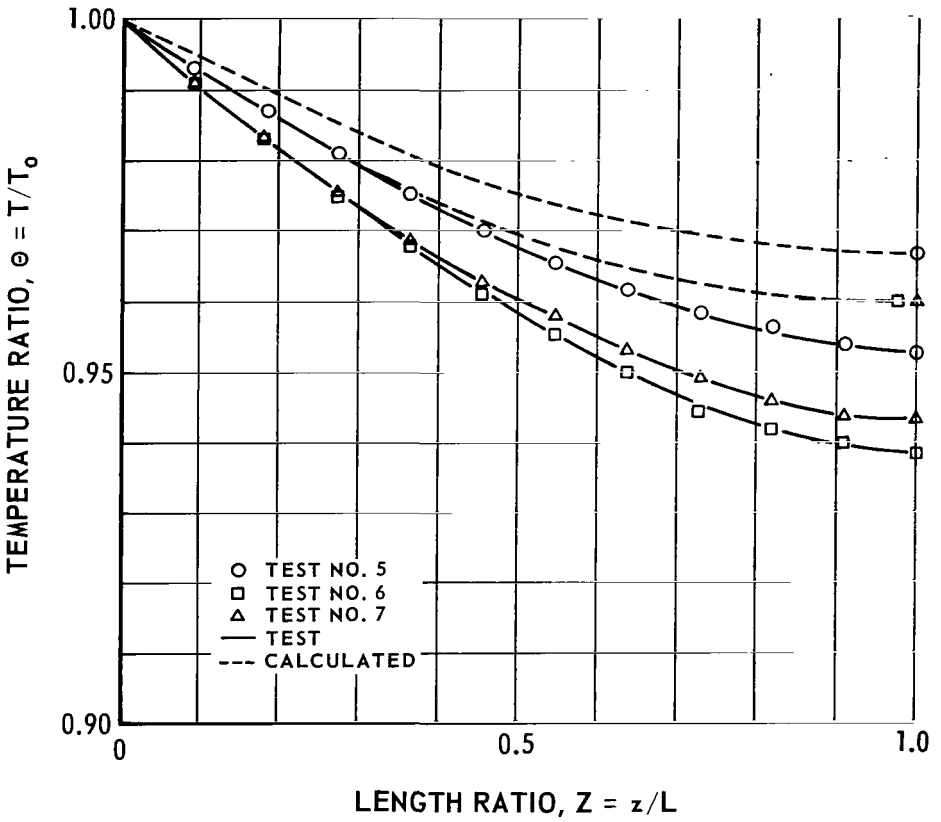

FIGURE C-5. TESTS 5-7 AND CALCULATED TEMPERATURE DISTRIBUTIONS FOR ROD WITH BASE (Uncoated)

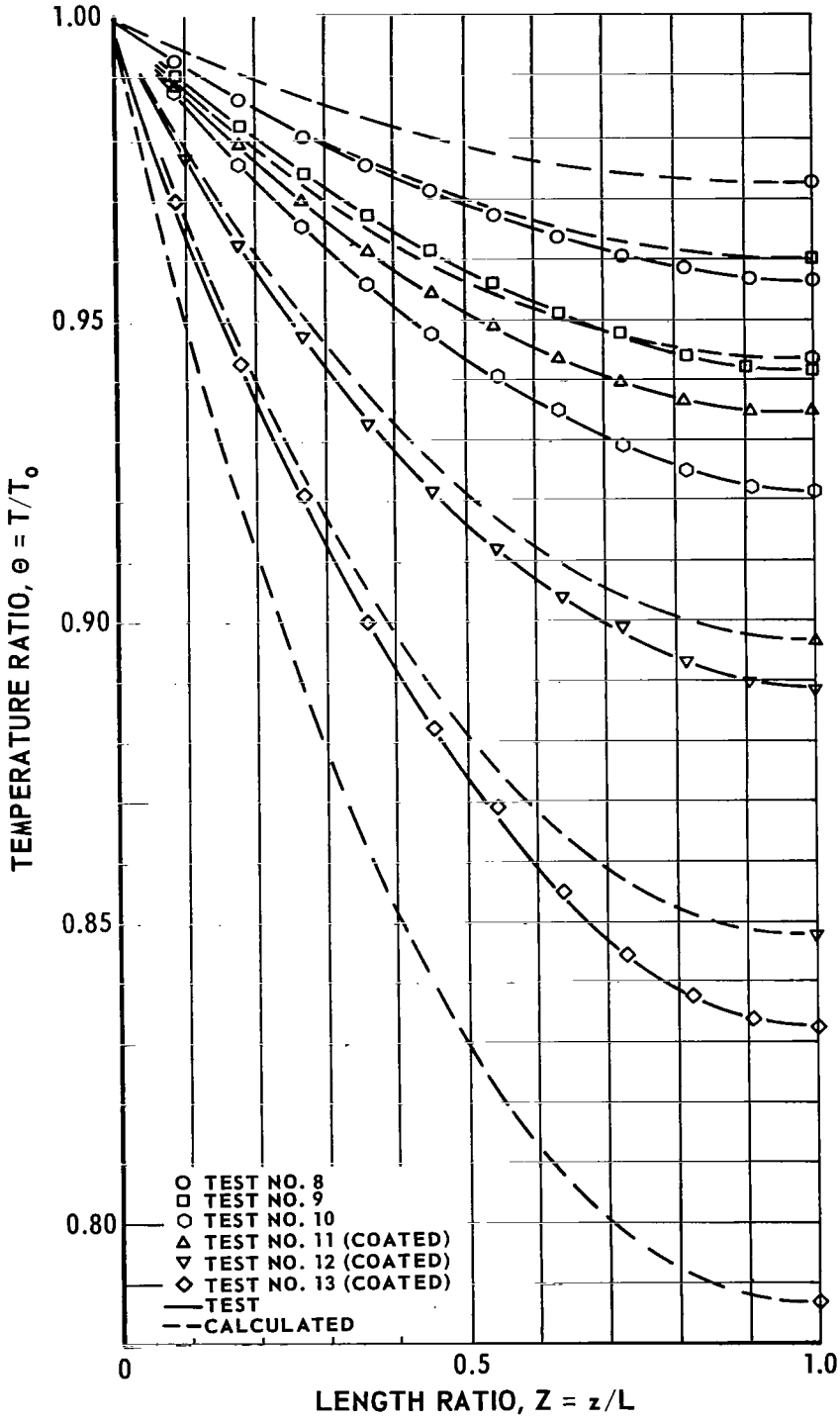

FIGURE C-6. TESTS 8-13 AND CALCULATED TEMPERATURE DISTRIBUTIONS FOR ROD WITH NO BASE (Coated and Uncoated)

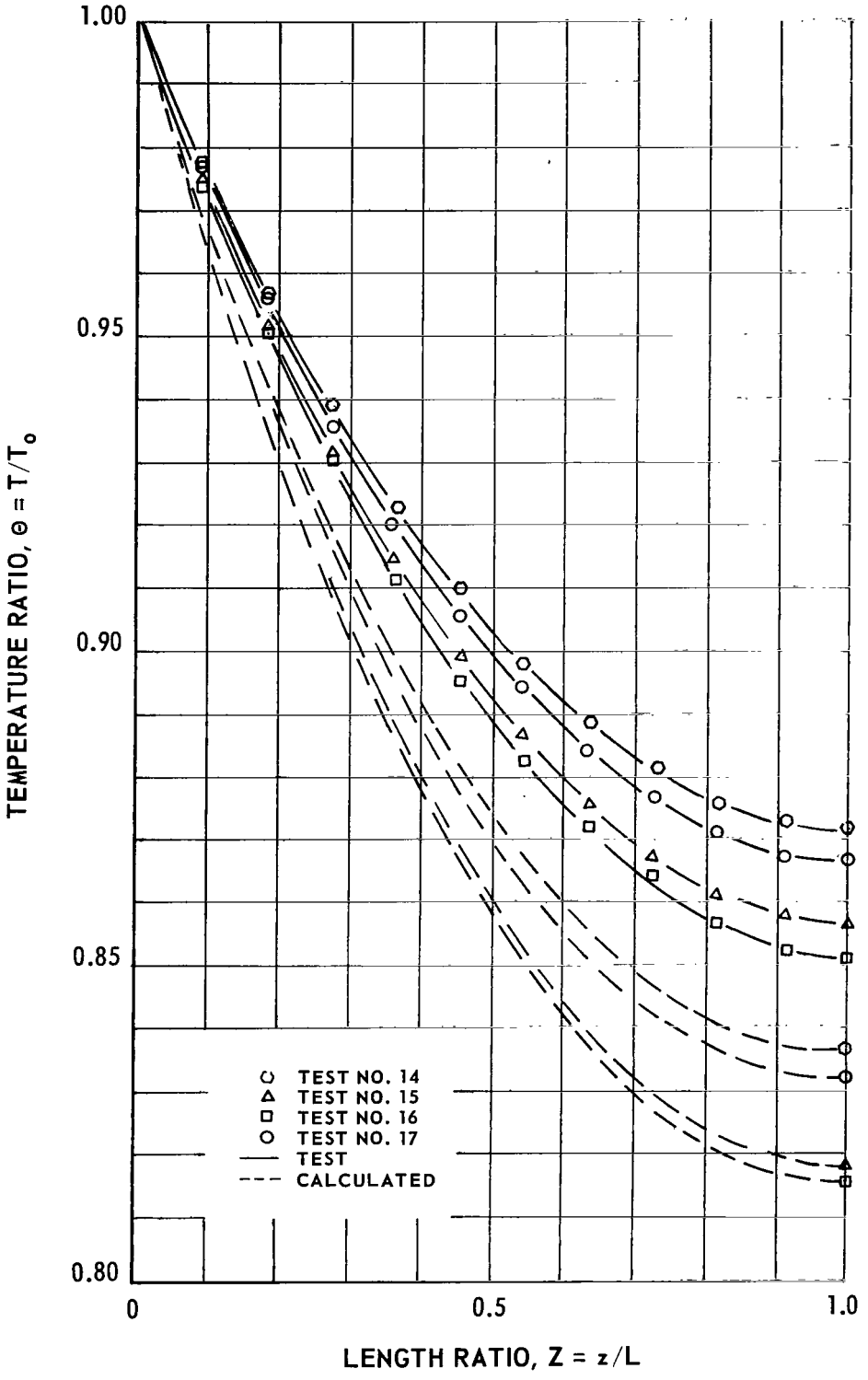

FIGURE C-7. TESTS 14-17 AND CALCULATED TEMPERATURE DISTRIBUTIONS FOR ROD WITH BASE (Coated)

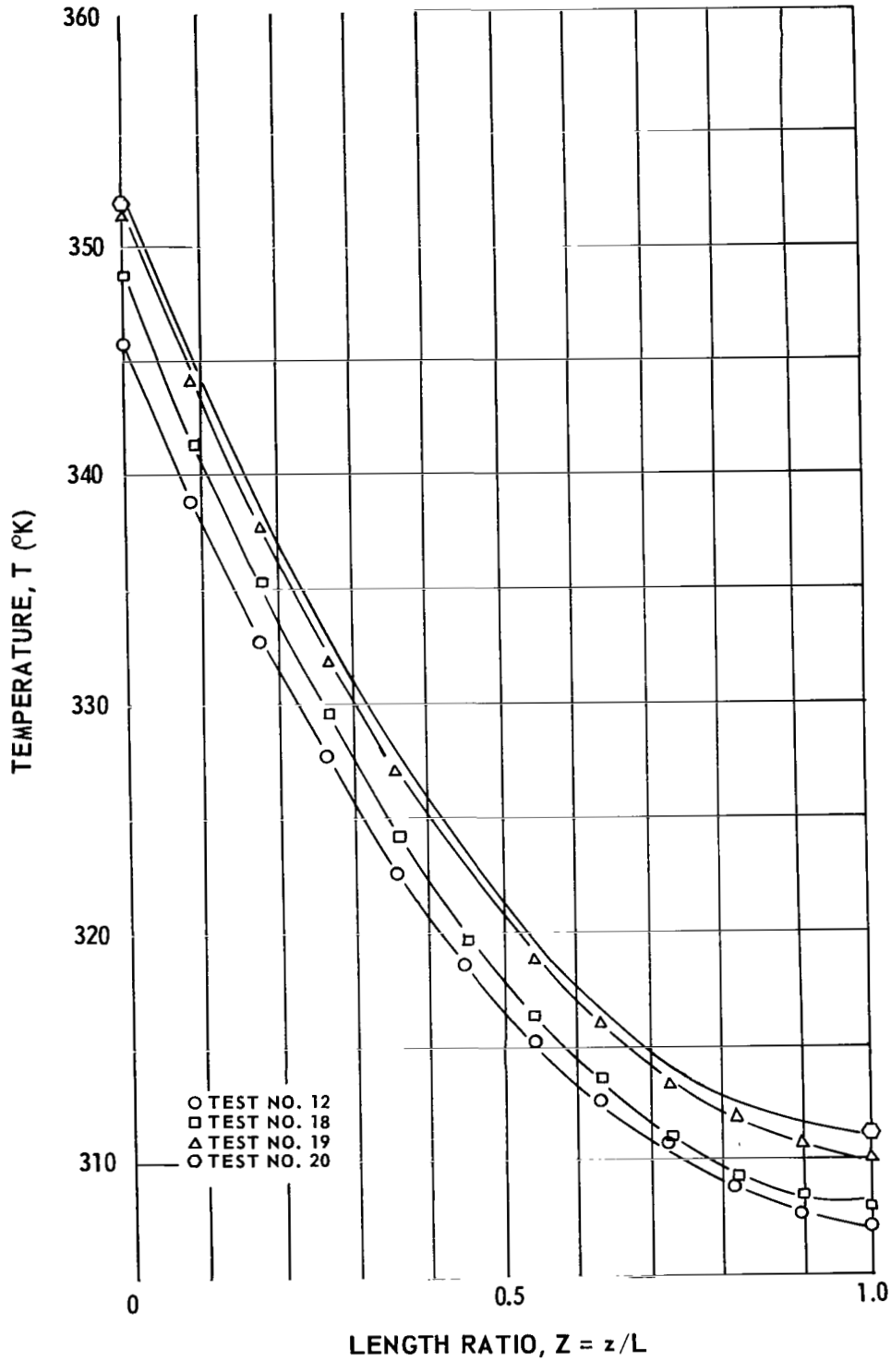

FIGURE C-8. TEMPERATURE DISTRIBUTIONS FOR THERMOCOUPLE CORRECTION TEST RUNS, T(°K) (Coated)

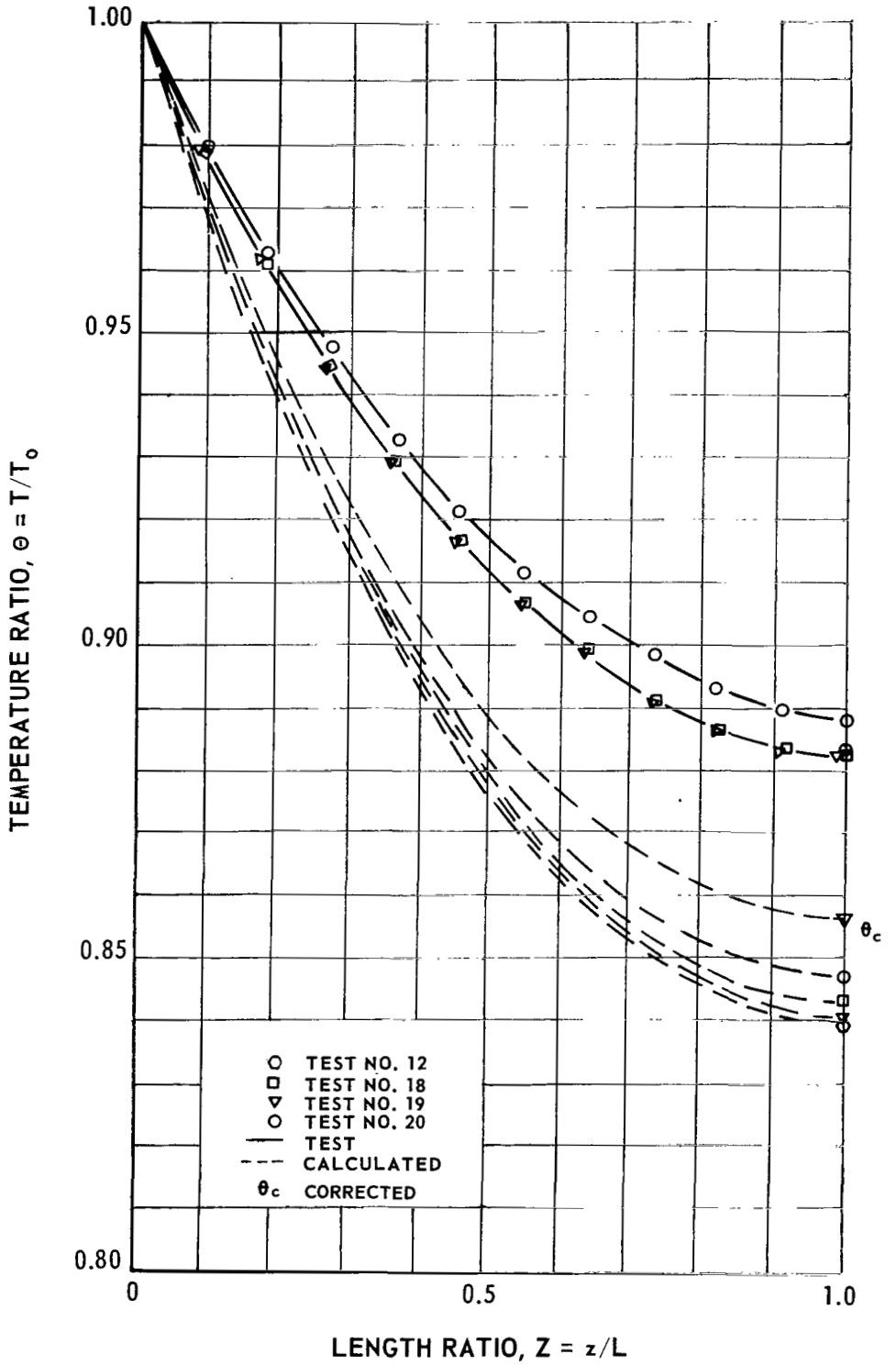

FIGURE C-9. TEMPERATURE DISTRIBUTIONS FOR THERMOCOUPLE CORRECTION TEST RUNS, $\theta = T/T_0$ (Coated)

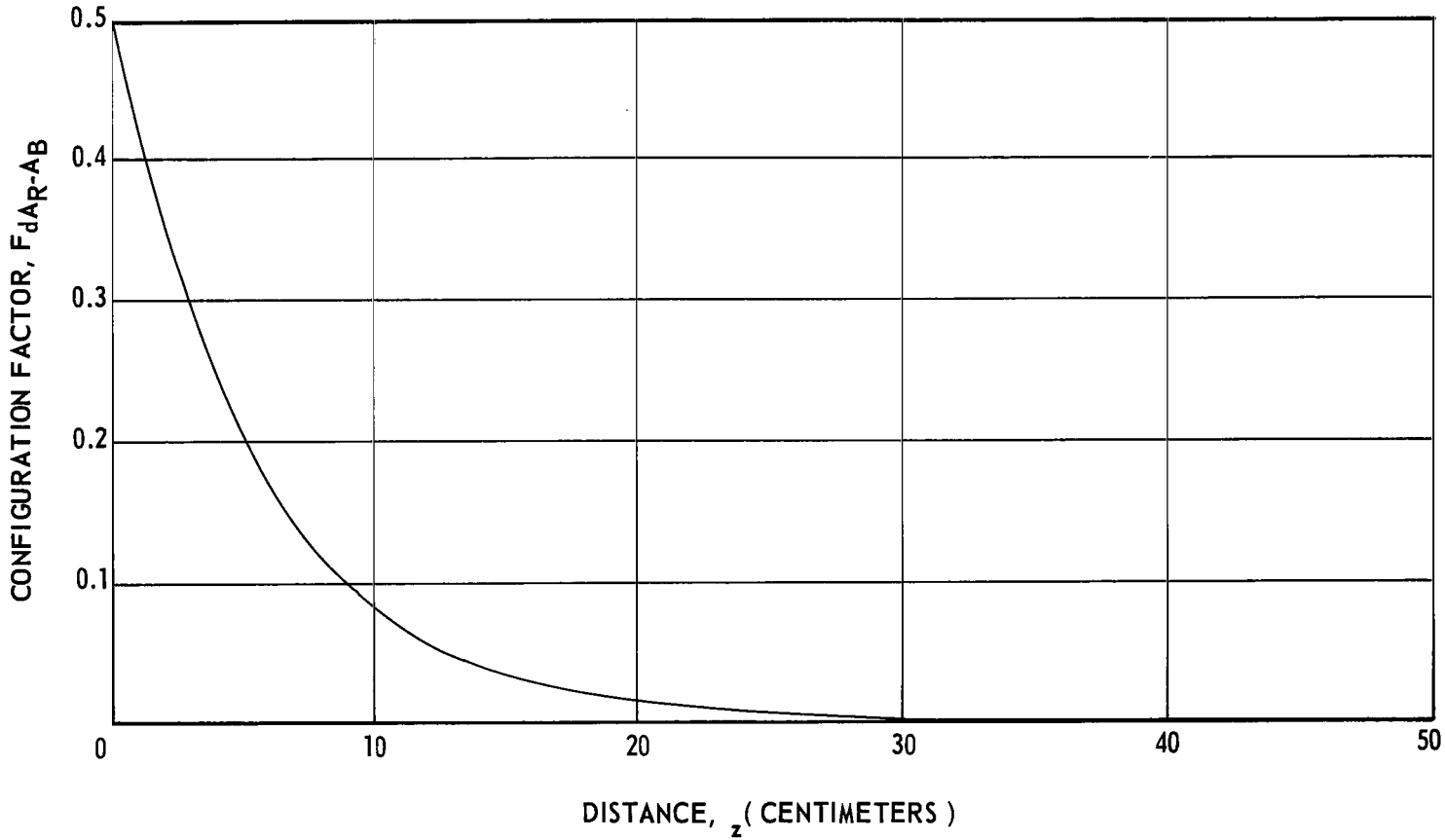

FIGURE C-10. CONFIGURATION FACTOR OF A DIFFERENTIAL ELEMENT OF ROD VIEWING BASE FROM DISTANCE z

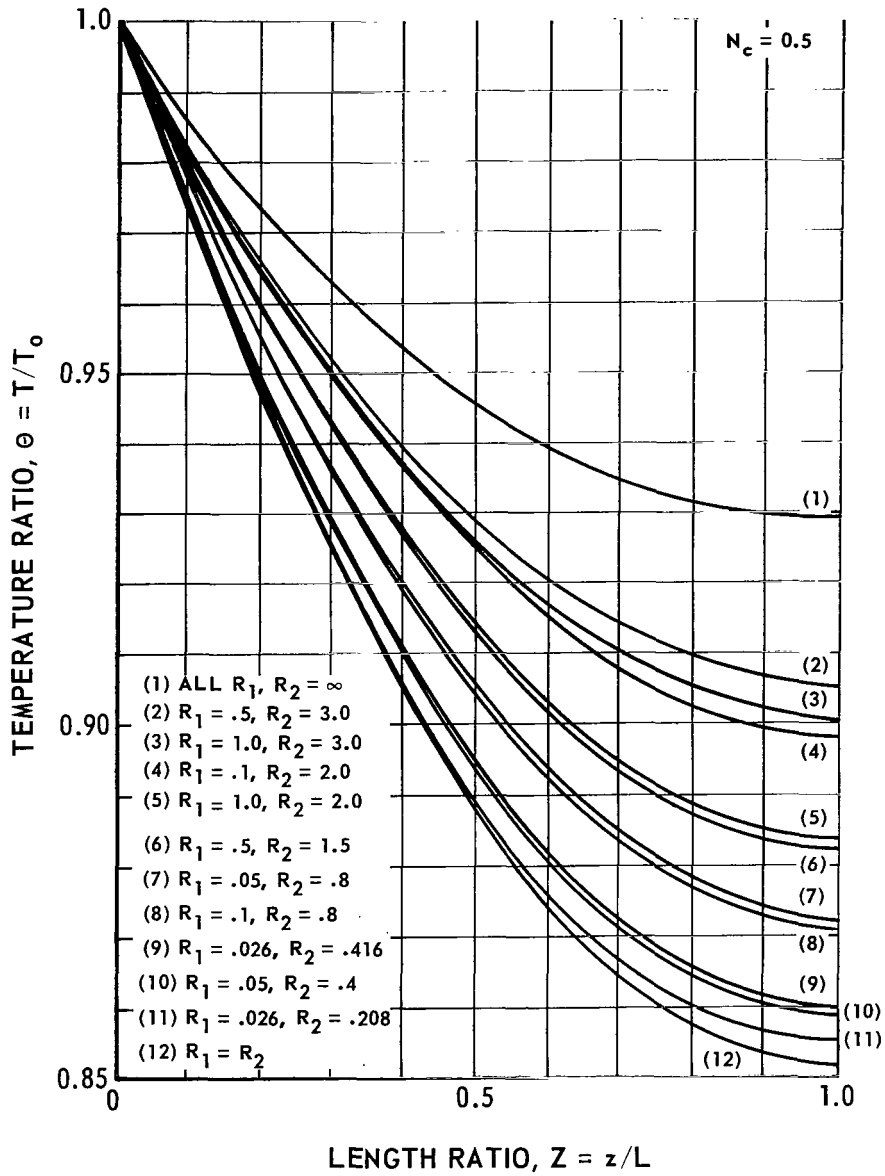

FIGURE C-11. TEMPERATURE DISTRIBUTIONS FOR FIXED N_C AND VARIOUS R_1 AND R_2 RATIOS (Black Surfaces)

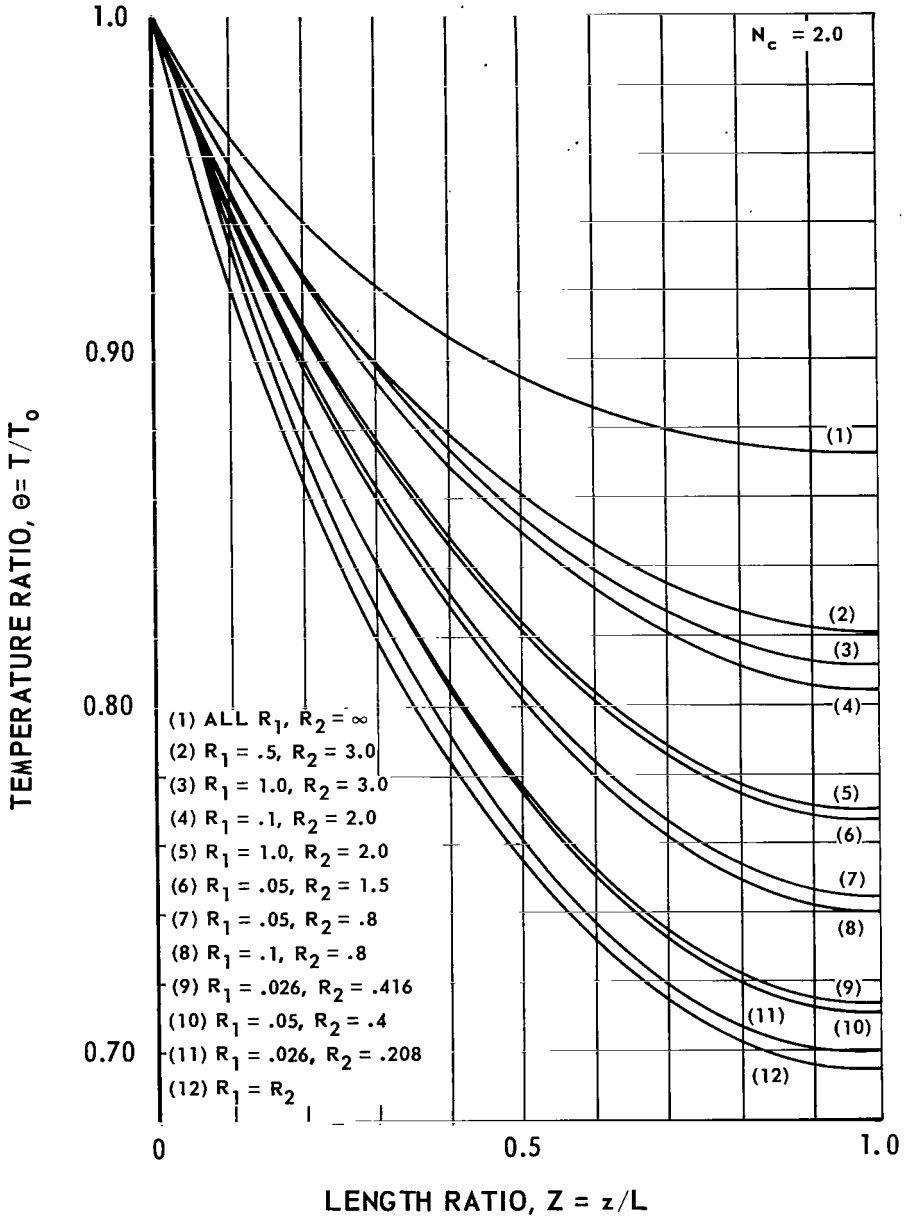

FIGURE C-12. TEMPERATURE DISTRIBUTION FOR FIXED N_c AND VARIOUS R_1 AND R_2 RATIOS (Black Surfaces)

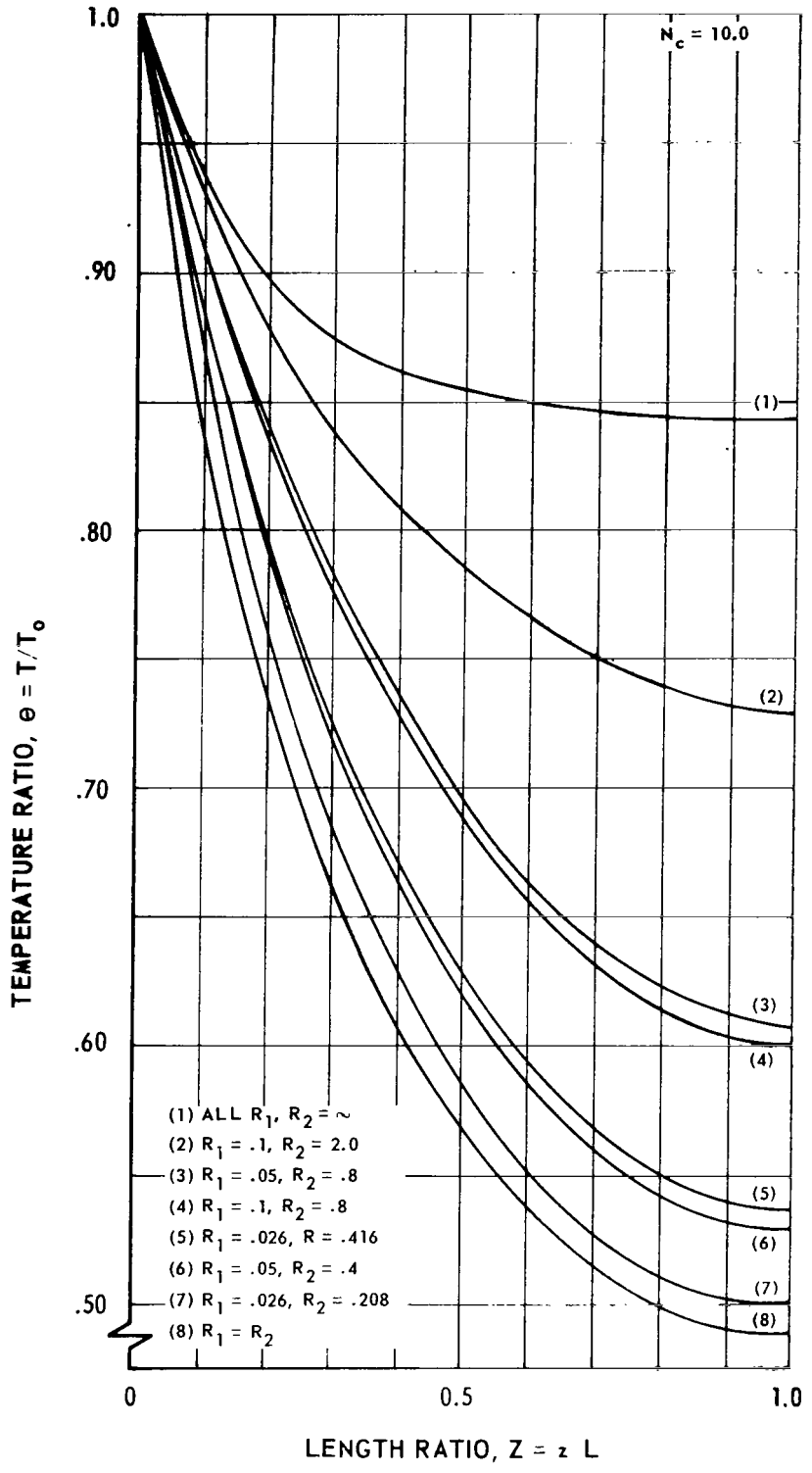

FIGURE C-13. TEMPERATURE DISTRIBUTIONS FOR FIXED N_C AND VARIOUS R_1 AND R_2 RATIOS (Black Surfaces)

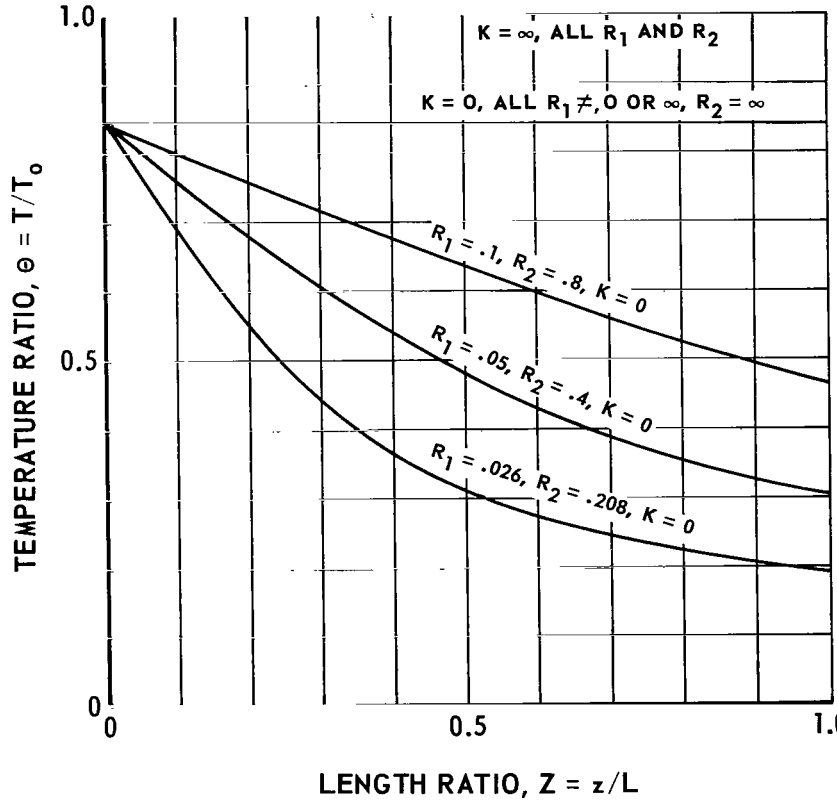

FIGURE C-14. SOME LIMITING CASES OF TEMPERATURE DISTRIBUTION FOR BLACK SURFACES

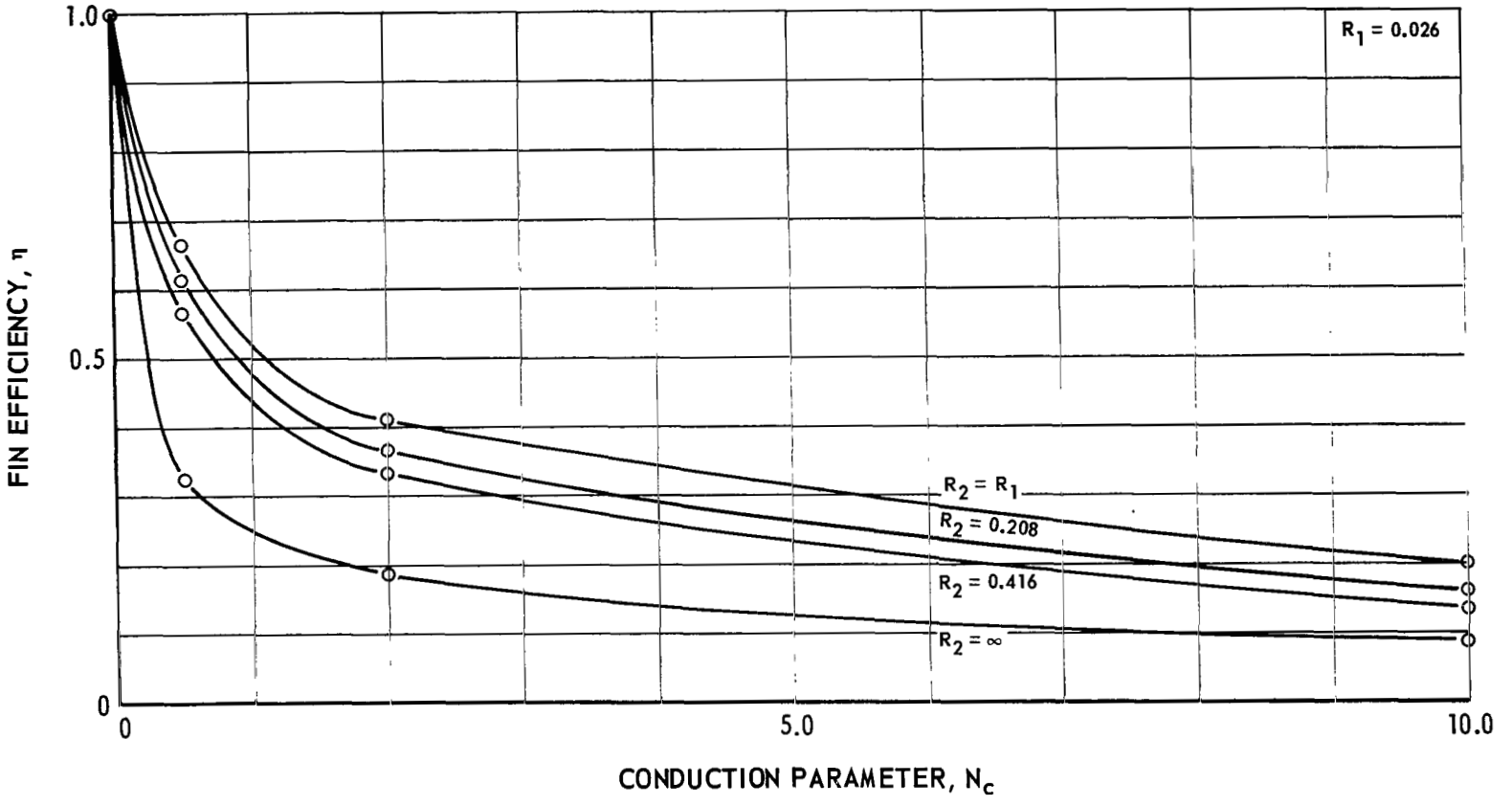

FIGURE C-15. FIN EFFICIENCY VARIATION WITH CONDUCTION PARAMETER FOR FIXED VALUES OF R_1 AND VARIOUS R_2 RATIOS, $R_1 = 0.026$ (Black Surfaces)

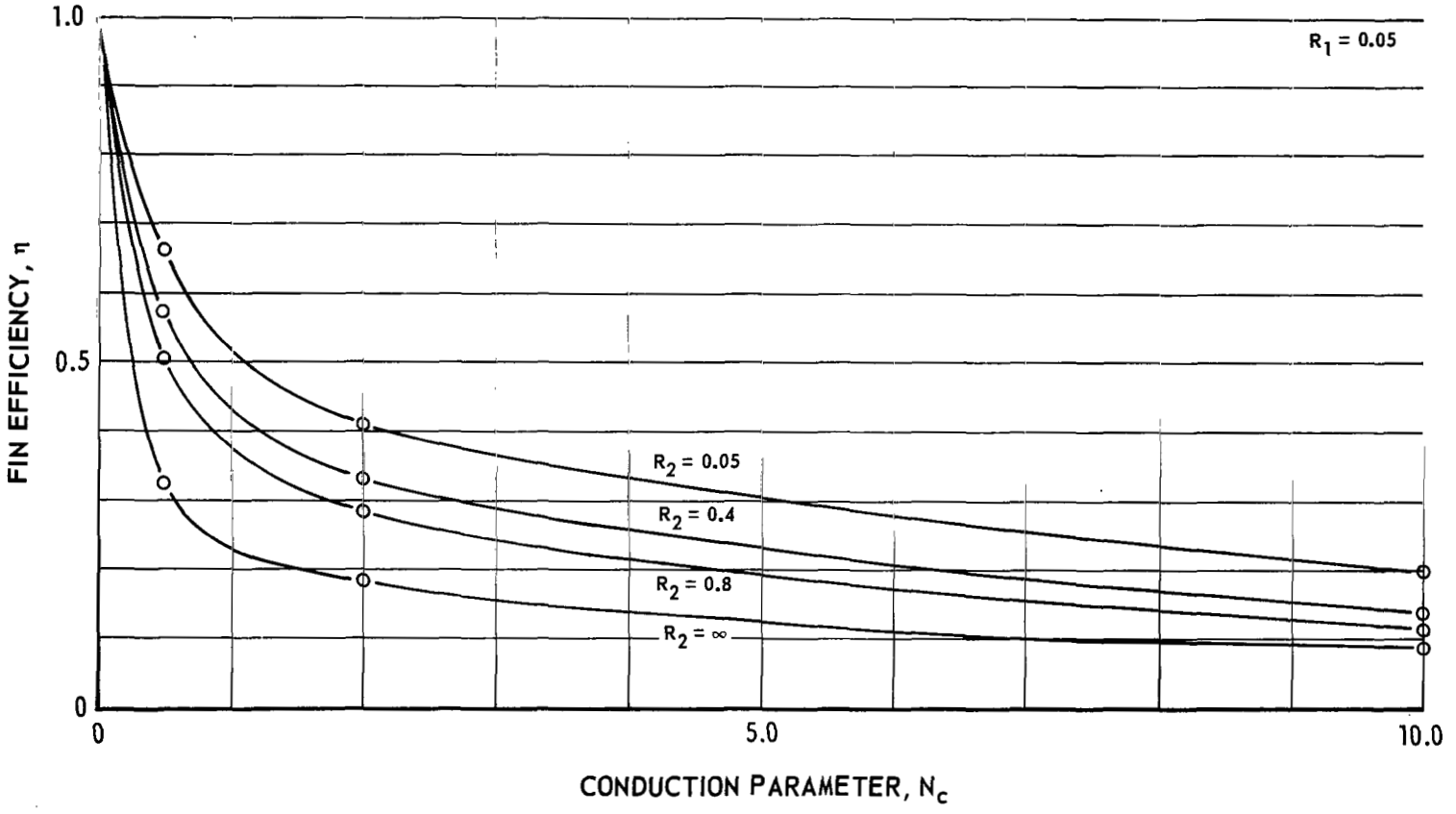

FIGURE C-16. FIN EFFICIENCY VARIATION WITH CONDUCTION PARAMETER FOR FIXED VALUES OF R_1 AND VARIOUS R_2 RATIOS, $R_1 = 0.05$ (Black Surfaces)

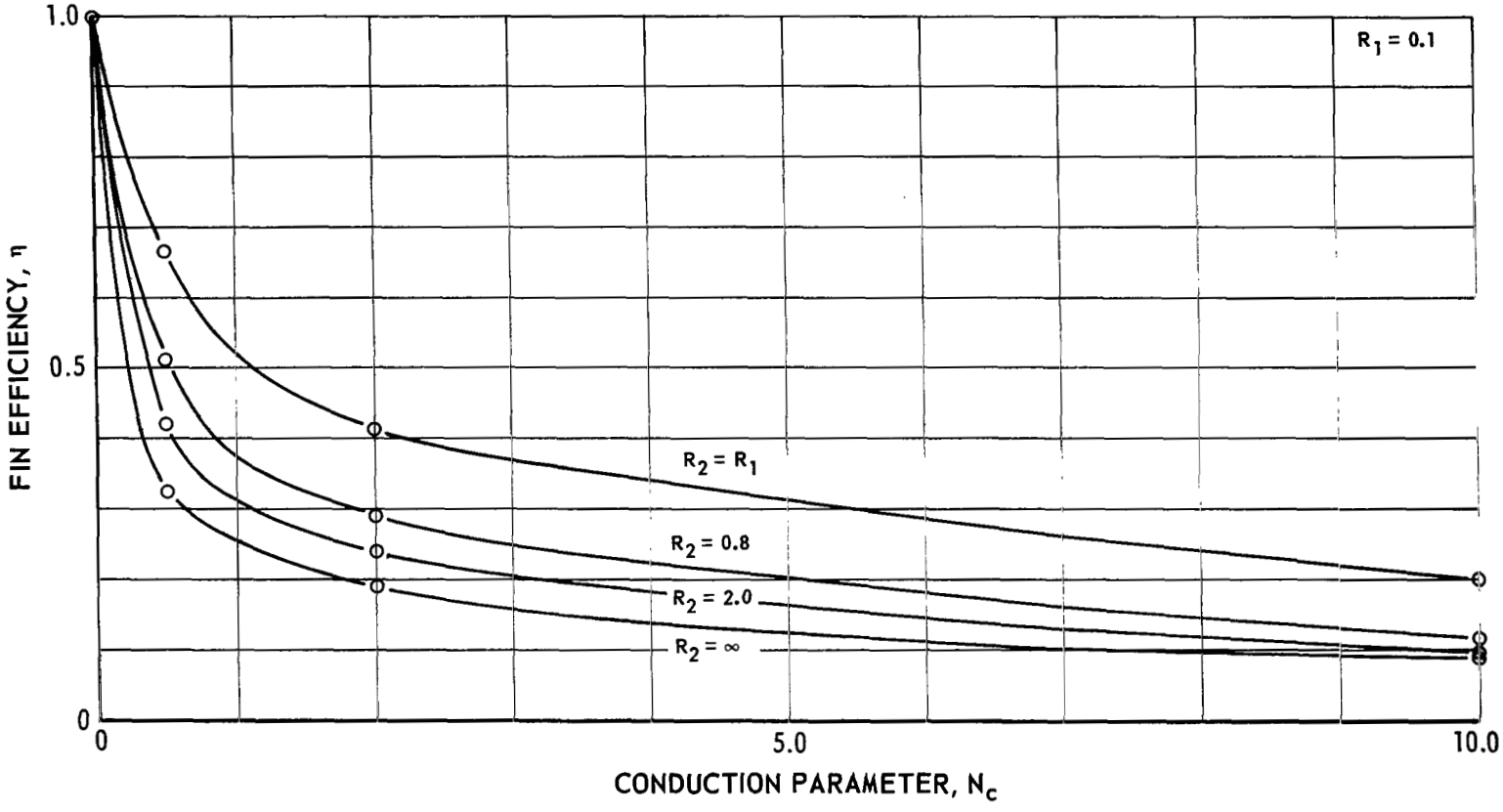

FIGURE C-17. FIN EFFICIENCY VARIATION WITH CONDUCTION PARAMETER FOR FIXED VALUES OF R_1 AND R_2 RATIOS, $R_1 = 0.1$ (Black Surfaces)

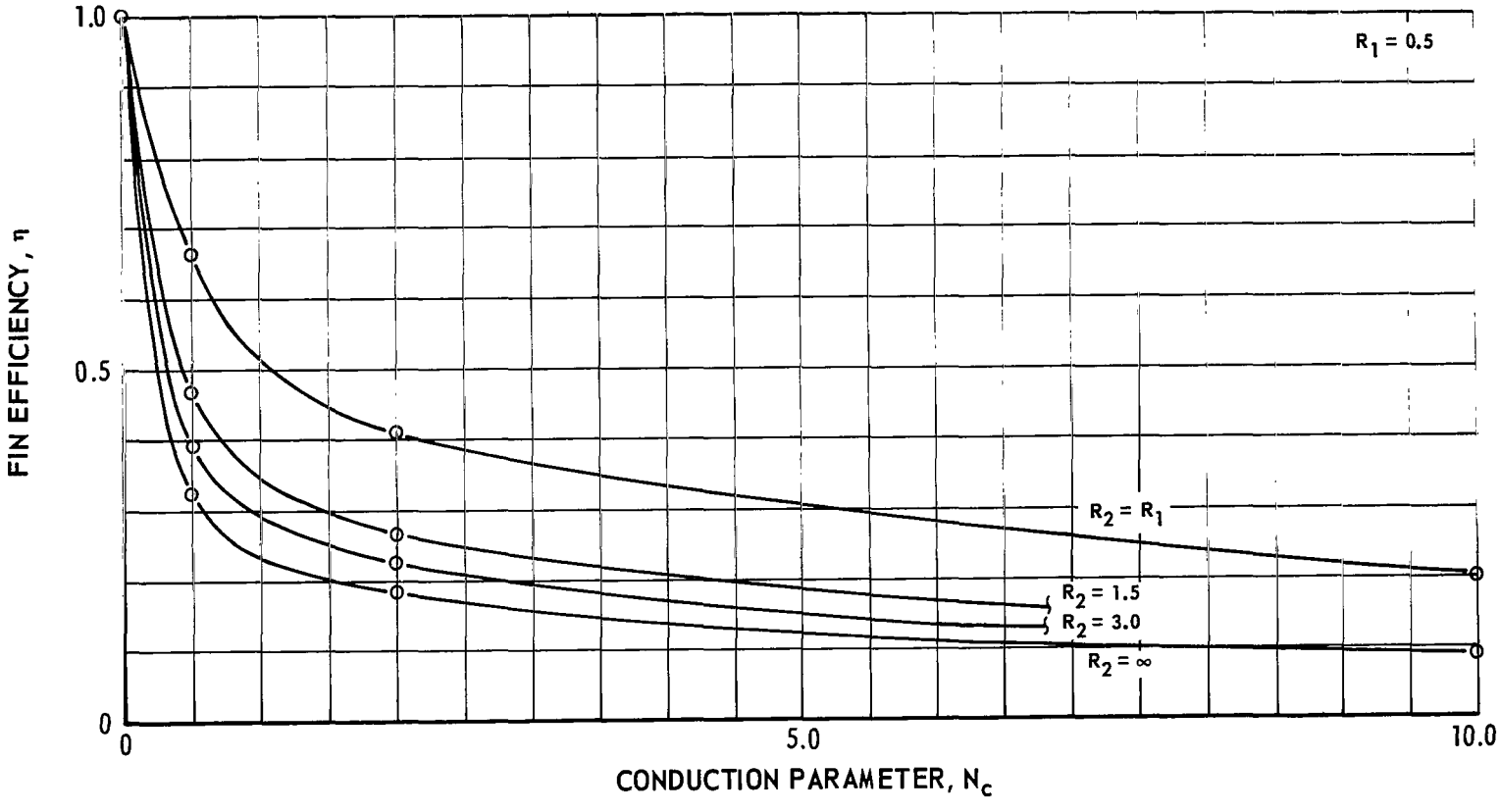

FIGURE C-18. FIN EFFICIENCY VARIATION WITH CONDUCTION PARAMETER FOR FIXED VALUES OF R_1 AND VARIOUS R_2 RATIOS, R = 0.5 (Black Surfaces)

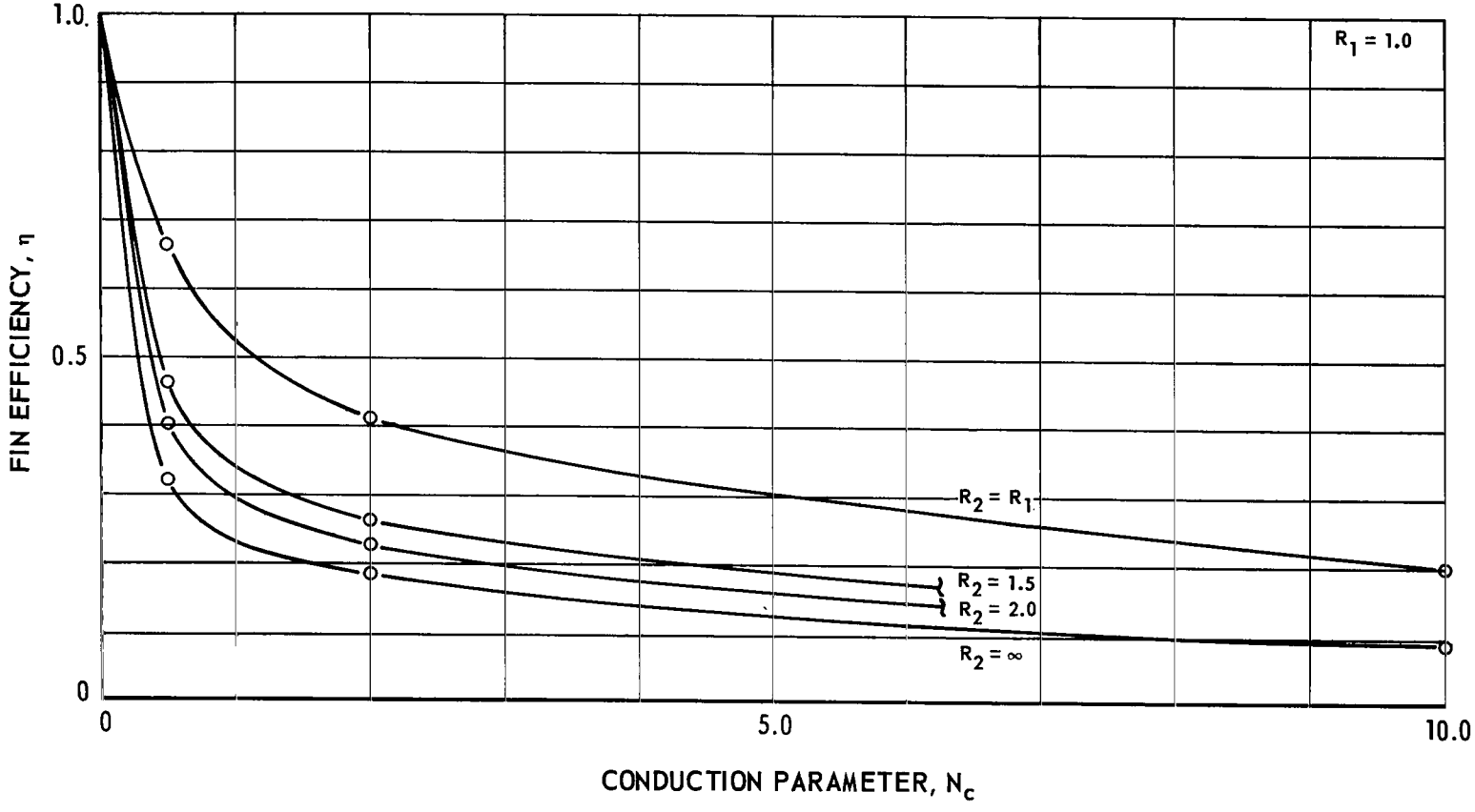

FIGURE C-19. FIN EFFICIENCY VARIATION WITH CONDUCTION PARAMETER FOR FIXED VALUES OF R_1 AND VARIOUS R_2 RATIOS, $R_1 = 1.0$ (Black Surfaces)

TABLE C-1. CALCULATED TEMPERATURE DISTRIBUTIONS

	Conduction Parameter, $N_c = 2.0$		
	$R_1 = 0.1$ and $R_2 = 0$	$R_1 = 0.1$ and $R_2 = 2.0$	$R_1 = 0.1$ and $R_2 = \infty$
Dimensionless Length, Z	Dimensionless Temperature, θ	Dimensionless Temperature, θ	Dimensionless Temperature, θ
0.0	1.00000	1.00000	1.00000
0.1	0.92712	0.95783	0.96708
0.2	0.86916	0.92324	0.94171
0.3	0.82271	0.89454	0.92212
0.4	0.78549	0.87064	0.90701
0.5	0.75591	0.85083	0.89546
0.6	0.73289	0.83468	0.88678
0.7	0.71566	0.82201	0.88048
0.8	0.70369	0.81274	0.87621
0.9	0.69664	0.80699	0.87374
1.0	0.69431	0.80496	0.87293

TABLE C-2. TEST SUMMARY

Test No.	Date	Rod Power (W)	Base Power (W)	Vacuum (mm of Hg)	Test Duration (Hours)
1	6/16/67	40.4	0	1.5×10^{-5}	6.5
2	7/11/67	40.4	0	4.0×10^{-7}	8.0
3	7/17/67	40.4	30.6	1.2×10^{-6}	8.0
4	7/19/67	40.4	42.2	2.0×10^{-6}	8.0
5	7/20/67	18.6	0	2.5×10^{-6}	8.0
6	7/21/67	18.6	22.5	3.0×10^{-6}	8.0
7	7/24/67	18.6	10.0	1.2×10^{-6}	8.0
8	7/25/67	18.6	No Base	1.5×10^{-6}	9.0
9	7/25/67	29.0	No Base	8.0×10^{-7}	12.6
10	7/26/67	40.4	No Base	8.0×10^{-7}	8.8
11	8/7/67[a]	18.1	No Base	7.0×10^{-7}	13.7
12	8/7/67[a]	41.6	No Base	5.0×10^{-7}	10.5
13	8/8/67[a]	75.3	No Base	3.0×10^{-7}	11.5
14	8/9/67[a]	41.8	10.0	5.0×10^{-7}	17.3
15	8/10/67[a]	41.6	62.5	8.0×10^{-7}	11.0
16	8/10/67[a]	41.6	90.0	8.0×10^{-7}	11.8
17	8/11/67[a]	40.4	22.5	3.0×10^{-7}	10.8
18	8/15/67[a]	41.6	No Base	1.2×10^{-6}	11.2
19	8/17/67[a]	41.6	No Base	1.5×10^{-6}	10.9
20	8/18/67[a]	41.6	No Base	9.0×10^{-7}	11.5

a. Denotes the specimen was carbon coated.

TABLE C-3. TEST DATA

Test Number	Temp. of Base ($T_B \sim$ °K)	Temp. of Rod At Base ($T_0 \sim$ °K)	N_c
1	393.0	508.6[a]	1.70488
2	365.2	457.4	1.24091
3	477.2	497.6	1.59716
4	512.9	503.4	1.65317
5	305.2	353.5	0.57264
6	427.8	380.5[a]	0.71391
7	407.3	380.5	0.71391
8	—	343.5	0.52541
9	—	389.9	0.76818
10	—	445.4	1.14507
11	—	280.6	0.28617
12	—	345.8	0.53601
13	—	423.6	0.98544
14	344.6	368.7	0.64961
15	449.9	394.4	0.79549
16	490.2	403.2	0.84957
17	367.2	377.2	0.69586
18	—	348.8	0.54987
19	—	351.4	0.56258
20	—	352.1	0.56579

a. Steady state conditions were marginal.

TABLE C-4. TEMPERATURE ERROR AT THE INSULATED END OF THE ROD

Test Number	Dimensionless Temperature, θ_{11}, of Rod (Test)	Dimensionless Temperature, θ_{11}, of Rod (Calculated)	% Error
1	0.9113	0.9169	-0.61
2	0.9159	0.9354	-2.09
3	0.9003	0.9210	-2.25
4	0.8988	0.9189	-2.19
5	0.9525	0.9667	-1.47
6	0.9381	0.9596	-2.24
7	0.9430	0.9596	-1.73
8	0.9560	0.9719	-1.64
9	0.9411	0.9597	-1.94
10	0.9210	0.9431	-2.34
11	0.9344	0.8960	+4.28
12	0.8883	0.8473	+4.84
13	0.8322	0.7865	+5.97
14	0.8717	0.8363	+5.42
15	0.8568	0.8181	+4.73
16	0.8512	0.8160	+4.31
17	0.8668	0.8323	+4.15
18	0.8829	0.8433	+4.70
19	0.8822	0.8408	+4.92
20	0.8840	0.8396	+5.29

LIST OF REFERENCES

1. Jacob, Max: Heat Transfer, Vol. I. John Wiley and Sons, Inc., New York, 1957, pp. 97 and 207-243.

2. Langmuir, Irving: Heat Conductivity of Tungsten at High Temperatures and the Wiedmann-Franz-Lorenz Relation, Physical Review, Vol. 7, No. 1, 1916, pp. 151-152.

3. Langmuir, Irving, and Taylor, John Bradshaw: The Heat Conductivity of Tungsten and the Cooling Effects of Leads Upon Filaments at Low Temperatures. Physical Review, Vol. 50, 1936, pp. 68-87.

4. Worthing, A. G.: Temperature Distribution in an Incandescent Lamp Filament in the Neighborhood of a Cooling Junction. Physical Review, Vol. 4, No. 6, 1916, pp. 524-534.

5. Worthing, A. G., and Holiday, D.: Heat. John Wiley and Sons, Inc., New York, 1948, p. 171.

6. Stead, G.: The Short Tungsten Filament as a Source of Light and Electrons. Journal of Instn. Elect. Engrs., Vol. 58, 1920, pp. 107-117.

7. Bush, V., and Gould, King E.: Temperature Distribution Along a Filament. Physical Review, Vol. 29, 1927, pp. 337-345.

8. Baerwald, H. G.: The Distribution of Temperature in a Cylindrical Conductor Electrically Heated in Vacuo. Phil. Mag., Vol. 21, No. 141, 1936, pp. 641-648.

9. Jain, S. C., and Krishnan, Sir K. S.: The Distribution of Temperature Along a Thin Rod Electrically Heated in Vacuo. Part I, Theoretical Proceedings of Royal Society, Series A, Vol. 222, 1954, pp. 167-180; Part II, Vol. 225, 1954, pp. 1-7; Part III, Vol. 225, 1954, pp. 7-18; Part IV, Vol. 225, 1954, pp. 19-32; Part V, Vol. 227, 1955, pp. 141-154; Part VI, Vol. 229, 1955, pp. 439-444.

10. Shouman, A. R.: Nonlinear Heat Transfer and Temperature Distribution Through Fins and Electric Filaments of Arbitrary Geometry with Temperature-Dependent Properties and Heat Generation. National Aeronautics and Space Administration, Washington, D. C., TN D-4257, January 1968, pp. 1-24.

LIST OF REFERENCES (Continued)

11. Lieblein, Seymour: Analysis of Temperature Distribution and Radiant Heat Transfer Along a Rectangular Fin of Constant Thickness. National Aeronautics and Space Administration, Washington, D. C., TN D-196, November 1959, pp. 1-18.

12. Chambers, R. L. and Somers, E. V.: Radiation Fin Efficiency for One-Dimensional Heat Flow in a Circular Fin. Trans. ASME, Vol. 81, 1959, pp. 327-329.

13. Tatom, J. W.: Steady-State Behavior of Extended Surfaces in Space. ARS Journal, Vol. 30, 1960, p. 118.

14. Callinan, J. P., and Berggren, W. P.: Some Radiator Design Criteria for Space Vehicles. Trans. ASME, Series C, Vol. 81, 1950, pp. 237-244.

15. Bartas, J. G., and Sellers, W. H.: Radiation Fin Effectiveness. Trans. ASME, Series C, Vol. 82, 1960, pp. 73-75.

16. Sparrow, E. M., Eckert, E. R. G., and Irvine, T. F., Jr.: Analytical Formulation for Radiating Fins with Mutual Irradiation. ARS Journal, Vol. 30, 1960, pp. 644-646.

17. Sparrow, E. M., Eckert, E. R. G., and Irvine, T. F., Jr.: The Effectiveness of Radiating Fins with Mutual Irradiation. Journal of the Aerospace Sciences, Vol. 28, 1961, pp. 763-772.

18. Karlekar, R. V., and Chao, B. T.: Mass Minimization of Radiating Trapezoidal Fins with Negligible Base Cylinder Interaction. Int. J. of Heat and Mass Transfer, Vol. 6, 1963, pp. 33-48.

19. Hering, R. G.: Radiative Heat Exchange Between Conducting Plates with Specular Reflection. Trans. ASME, Series C, Vol. 88, 1966, pp. 29-36.

20. Sparrow, E. M., and Eckert, E. R. G.: Radiant Interaction Between Fin and Base Surfaces. Trans. ASME, Series C, Vol. 84, 1962, pp. 12-18.

21. Sarabia, M. F., and Hitchcock, J. E.: Heat Transfer from Gray Fin-Tube Radiators. Trans. ASME, Series C, Vol. 88, 1966, pp. 338-340.

LIST OF REFERENCES (Concluded)

22. Hwang-Bo, H.: Optimization of Some Radiators with Fins and Involute Reflectors. Trans. ASME, Series C, Vol. 89, 1967, pp. 99-102.

23. Sparrow, E. M., Miller, G. B., and Jonsson, V. K.: Radiating Effectiveness of Annular-Finned Space Radiators, Including Mutual Irradiation Between Radiator Elements. Journal of the Aerospace Sciences, Vol. 29, No. 1, 1962, pp. 1291-1298.

24. Gordon, G. D.: Measurement of Ratio of Absorptivity of Sunlight to Thermal Emissivity. The Review of Scientific Instruments, Vol. 31, No. 11, 1960, p. 1207.

25. Schnieder, P. J.: Conduction Heat Transfer. Addison-Wesley Publishing Company, Inc., Reading, Massachusetts, 1957, pp. 3 and 4.

26. Sparrow, E. M., and Cess, R. D.: Radiation Heat Transfer. Brooks/Cole Publishing Company, Belmont, California, 1966, pp. 86-90, pp. 113-126, and pp. 170-176.

27. Herriot, J. G.: Methods of Mathematical Analysis and Computation. John Wiley and Sons, Inc., New York, 1963, pp. 23-24.

28. Dwight, H. B.: Tables of Integrals and Other Mathematical Data. The Macmillan Company, New York, 1957.

NASA-Langley, 1970 —— 33 M362

NATIONAL AERONAUTICS AND SPACE ADMINISTRATION
WASHINGTON, D.C. 20546
OFFICIAL BUSINESS

FIRST CLASS MAIL

POSTAGE AND FEES PAID
NATIONAL AERONAUTICS AN
SPACE ADMINISTRATION

POSTMASTER: If Undeliverable (Section 158 Postal Manual) Do Not Return

"The aeronautical and space activities of the United States shall be conducted so as to contribute . . . to the expansion of human knowledge of phenomena in the atmosphere and space. The Administration shall provide for the widest practicable and appropriate dissemination of information concerning its activities and the results thereof."

—NATIONAL AERONAUTICS AND SPACE ACT OF 1958

NASA SCIENTIFIC AND TECHNICAL PUBLICATIONS

TECHNICAL REPORTS: Scientific and technical information considered important, complete, and a lasting contribution to existing knowledge.

TECHNICAL NOTES: Information less broad in scope but nevertheless of importance as a contribution to existing knowledge.

TECHNICAL MEMORANDUMS: Information receiving limited distribution because of preliminary data, security classification, or other reasons.

CONTRACTOR REPORTS: Scientific and technical information generated under a NASA contract or grant and considered an important contribution to existing knowledge.

TECHNICAL TRANSLATIONS: Information published in a foreign language considered to merit NASA distribution in English.

SPECIAL PUBLICATIONS: Information derived from or of value to NASA activities. Publications include conference proceedings, monographs, data compilations, handbooks, sourcebooks, and special bibliographies.

TECHNOLOGY UTILIZATION PUBLICATIONS: Information on technology used by NASA that may be of particular interest in commercial and other non-aerospace applications. Publications include Tech Briefs, Technology Utilization Reports and Notes, and Technology Surveys.

Details on the availability of these publications may be obtained from:

SCIENTIFIC AND TECHNICAL INFORMATION DIVISION

NATIONAL AERONAUTICS AND SPACE ADMINISTRATION

Washington, D.C. 20546